UNIVERSITY OF ZAGREB
FACULTY OF SCIENCE
DEPARTMENT OF PHYSICS

Ana Petrinec

TRANSIENT CURRENT TECHNIQUE (TCT) CHARACTERIZATION OF HIGH-ENERGY PHOTON IRRADIATED SILICON DETECTORS

Master Thesis

Zagreb, 2018.

SVEUČILIŠTE U ZAGREBU
PRIRODOSLOVNO-MATEMATIČKI FAKULTET
FIZIČKI ODSJEK

Ana Petrinec

KARAKTERIZACIJA SILICIJSKIH DETEKTORA OZRAČENIH VISOKOENERGETSKIM FOTONIMA METODOM TRANZIJENTNE STRUJE (TCT)

Diplomski rad

Zagreb, 2018.

UNIVERSITY OF ZAGREB
FACULTY OF SCIENCE
DEPARTMENT OF PHYSICS

INTEGRATED UNDERGRADUATE AND GRADUATE UNIVERSITY PROGRAMME IN PHYSICS

Ana Petrinec

Master Thesis

TRANSIENT CURRENT TECHNIQUE (TCT) CHARACTERIZATION OF HIGH-ENERGY PHOTON IRRADIATED SILICON DETECTORS

Advisor: Professor Jaakko Härkönen, dr.sc.

Co-Advisor: Professor Mihael Makek, doc.dr.sc.

Master Thesis grade: _____

Committee: 1. _____

2. _____

3. _____

Master Thesis defence date: _____

Zagreb, 2018.

I would like to thank my mentor prof.dr.sc. Jaakko Härkönen for support, advice and expert assistance in the development of this master thesis. I would like to offer my very special thanks to dr.sc. Aneliya Karadzhinova-Ferrer for her patience, guidance and accessibility. Advice given by dr.sc. Matti Kalliokoski has been a great help in data analysis. Thank you all for making me part of your team. Finally, I would like to thank those closest to me for their great support and understanding throughout my study.

Karakterizacija silicijskih detektora ozračenih visokoenergetskim fotonima metodom tranzijentne struje (TCT)

Sažetak

Kroz različite interakcije upadno zračenje materiji predaje energiju. To može oštetiti pravilnu kristalnu strukturu čime se narušavaju svojstva poluvodičkog detektora. Svrha je ovog rada proučavanje utjecaja ozračivanja visokoenergijskim gama zrakama na svojstva silicijskih detektora. Korišteni uzorci su diode n- i p-tipa napravljene od Czochralskog silicija u finskom centru za mikro- i nanotehnologiju Micronova. Za karakterizaciju detektora korištena je metoda tranzijentne struje (TCT) s crvenim i infracrvenim laserom (valnih duljina 660 i 1064 nm). Iz dobivenih signala mogu se, među ostalim, dobiti informacije o prikupljenom naboju, radnom naponu, raspodjeli električnog polja unutar volumena detektora i predznaku prostornog naboja u zoni osiromašenja. S porastom primljene doze zračenja detektoru se mijenja napon potpunog osiromašenja, gubi naboj te dolazi do porasta struje kroz detektor u nepropusnoj polarizaciji. Na maksimalnoj dozi kojom su detektori ozračeni (187 kGy) jedina sa sigurnošću uočena posljedica bila je porast struje u neropusnoj polarizaciji. Detektori n-tipa pokazali su se otpornijima na gama zračenje od detektora p-tipa.

Ključne riječi: silicijski detektori zračenja, metoda tranzijentnih struja (TCT), otpornost na zračenje

Transient Current Technique (TCT) characterization of high-energy photon irradiated silicon detectors

Abstract

Incident radiation delivers energy to matter through different interactions. This can disrupt regular crystal structure of a semiconductor detector, which degrades its properties. The purpose of this thesis is to study the effect of gamma radiation on the properties of silicon detectors. Samples used are n- and p-type diodes made of Czochralski silicon. They were produced in Finnish Center for Micro- and Nanotechnology Micronova. Transient Current Technique (TCT) with red and infrared laser (wavelengths 660 and 1064 nm) is used to characterize the detectors. From recorded transients the information can be obtained about collected charge, full depletion voltage, electric field distribution and sign of the space charge, to name a few. With increasing radiation dose, detector may experience charge loss, full depletion voltage changes and an increase in the leakage current. For maximum dose at which detectors were irradiated (187 kGy), the only observable effect was increase of the leakage current. N-type detectors proved to be more resilient to gamma irradiation than p-type one.

Keywords: silicon detectors, transient current technique (TCT), radiation hardness

Contents

1 Introduction

Semiconductor diode detectors became practically available around 1960s when they provided the first high-resolution energy measurements. In the beginning they were implemented in nuclear physics research, specifically in charged particle detection and gamma spectroscopy, since their high density offers greater detection efficiency even with small detector sizes (compared to e.g. gas detectors) [1]. Furthermore, semiconductor detectors in general offer superior energy resolution. The energy resolution depends on number of information carriers and in semiconductors electron-hole pairs (ehps) play that role. Average energy needed to excite one ehp is of the order of few eV, which is between one and two orders of magnitude less than what is needed to excite information carrier in a scintillation counter. Other desirable features of semiconductor detectors are relatively fast timing characteristics, variable effective thickness, very thin entrance windows and simplicity of operation [2]. In time, semiconductor detectors gained attention for their potential uses in high-energy physics, and were eventually implemented in many different experiments. Innermost tracking system of large particle detectors (e.g. CERN Compact Muon Solenoid) is usually made of multiple layers of silicon detectors. The typical layout of one such detector system is presented in figure 1.1.

However, one of the drawbacks of semiconductor detectors is relatively high susceptibility to performance degradation from radiation-induced damage [2]. In order to estimate how long the particle tracker system would stay operational, it is necessary to examine detector behaviour after they are exposed to radiation. Transient current technique (TCT) is one of the commonly used methods for detector characterization that has been studied in detail and implemented in this thesis. It is based on the analysis of laser-induced current pulses arising from the drift of non-equilibrium ehps in the sensitive region of the detector. The excitation of the ehps can be achieved by red (λ = 660 nm) or infrared (λ = 1064 nm) picosecond laser pulses, or by a radioactive source. Different laser light penetration depths in combination with back or front side illumination offer a chance to study different transients (electron dominated, hole dominated, or consisting of both electrons and holes). The data obtained from TCT measurements can be used to determine various device parameters, such as collected charge, full depletion voltage, electric field distribution and the sign of

space charge, charge collection efficiency and effective trapping time [3]. Exposure to radiation affects many of the mentioned characteristics in ways detrimental to detector operation. Years of research in effort to increase radiation hardness yielded three approaches - material engineering, device engineering and variation of detector operational conditions [4]. This work focuses on Czochralski silicon (Cz-Si) diode detector operated in reverse bias mode. Silicon (Si) diodes have 1.115 eV band gap at 300 K and 3.62 eV is needed for the creation of one ehp, which makes them suitable for use at room temperatures. Even though current research in developing radiation hard Si detectors is highly focused on their implementation in next generation high-luminosity Large Hadron Collider (HL-LHC) experiments, these technologies will find its application across many different fields, besides high-energy physics. For example, during the extraterrestrial missions the satellite maintenance is not possible, so longer reliable detection lifetime which comes with improved radiation hardness is very valuable. As another example, in medical dosimetry radiation hard Si detectors could prove as simple, more resilient and much more cost-efficient alternative to currently used Thermally Luminescent Dosimeters.

The work presented in this thesis is done at the Ruđer Bošković Institute (RBI) in a framework of the European Union, Horizon 2020, European Research Area (ERA) program and Particle and Radiation Detectors, Sensors and Electronics in Croatia (PaRaDeSeC) project. The work is done in collaboration with Helsinki Institute of Physics (HIP) and Micronova Nanofabrication Centre. Micronova is Finland's National Research Infrastructure for micro- and nanotechnology, jointly run by VTT Technical Research Centre of Finland and Aalto University.

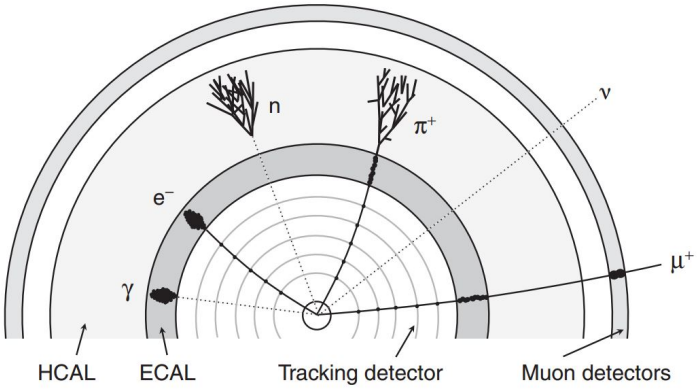

Figure 1.1: Typical layout of a large particle physics detector consists of a tracking system (here shown with cylindrical layers of a silicon detector), an electromagnetic calorimeter, a hadron calorimeter and muon detectors [12].

2 The pn-junction silicon particle detector

In order to construct a functional semiconductor radiation detector it is necessary to use appropriate contact electrodes at the boundaries of sensitive volume that will allow separation and collection of radiation induced electrons and holes. If a silicon device is operated as a resistor with ohmic contacts, charges of either sign can flow freely through it. The equilibrium charge carrier concentration is maintained in the semiconductor, which results in high steady-state leakage current. For the highest purity silicon the resistivity is around 50 kΩcm. Leakage current through e.g. 1 mm thick silicon slab with surface area of 1 cm^2 would be as high as 0.1 A when biased to 500 V. In comparison, standard radiation induced current is in the order of few microamperes. Radiation detectors are typically not operated as resistors but rather as reverse biased pn-junction (see figure 2.1) or Schottky-junction diodes [2].

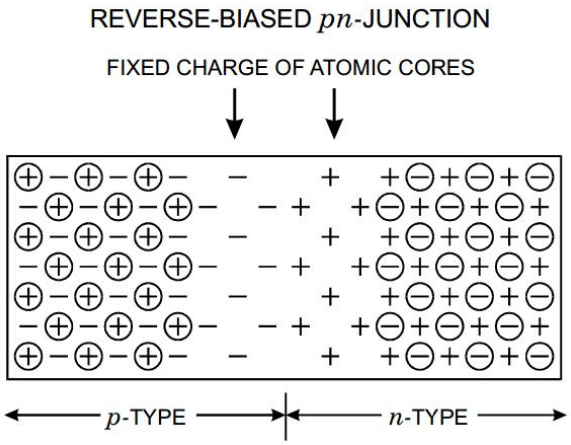

Figure 2.1: Illustration shows formation of the depletion region at the pn-junction, with fixed space charge distribution left behind after charge compensation [6].

Blocking electrodes are used to reduce the magnitude of the current through the bulk of the semiconductor and the natural choice is pn-junction. When p-type and n-type semiconductor materials come in contact, depletion region void of free charge carriers is formed, as illustrated in figure 2.1 (see section 2.1 for more details). Fixed space charge distribution that is left behind in the depletion region forms electric field across the junction, which restricts the movement of electrons and holes to opposite directions. Reverse biasing only accentuates this effect. That way, charge carriers removed at one electrode cannot be replaced at the opposite electrode, and their overall concentration within semiconductor will drop after application of an electric field. This can reduce leakage current enough to allow detection of additional current

pulse produced by the passage of radiation [2].

2.1 Pn-junction and forming of the depletion region

P-type semiconductors are doped with acceptor impurities such as gallium, boron and indium which have excess of hole charge carriers, while n-type semiconductors are doped with donor impurities such as arsenic, phosphorous or antimony, which introduce excess of electron charge carriers [1]. In practice, pn-junction is made by implanting one type of impurities in semiconductor crystal already doped with impurities of the opposite type. In the example illustrated in figure 2.2 donor impurities N_D are ion implanted in p-type crystal until their near surface concentration exceeds the acceptor impurities concentration N_A already present. This area of the crystal, where that condition is fulfilled, converts to n-type. Figure 2.2a illustrates an example of concentration profile. Intrinsic electron and hole concentrations in intrinsic semiconductor are labeled n_i and p_i. Initial acceptor concentration in p-type material is labeled N_A and profile of diffused donor impurities labeled by N_D is illustrated by thick black curve. This results in the formation of two regions with different concentration of electrons and holes on both sides of the junction. In the n-type region there is abundance of conduction electrons, in comparison to the p-type side. Such sharp gradient leads to electrons diffusing to p-type side where they recombine with holes. Or rather, electrons are captured by the vacancies in the covalent bonds of acceptor impurities on the p-type side of the junction, thus creating fixed negative space charge region. Analogue process affects the holes in the p-type region. Their concentration gradient leads to them diffusing towards n-type side where they recombine with electrons of donor impurities. Combined effect is build up of fixed negative space charge on p-type side and fixed positive space charge on n-type side of the pn-junction. Diffusion continues until electric field created by the space charges becomes just enough to compensate for further diffusion. For assumed doping concentration in figure 2.2a, space charge profile after carrier distribution reaches equilibrium is shown in figure 2.2b. This region of space charge imbalance is called depletion region. If one side of the junction is more doped than the other, its dominant charge carriers diffuse further into the opposite side. Therefore, depletion region extends further into the lightly doped side.

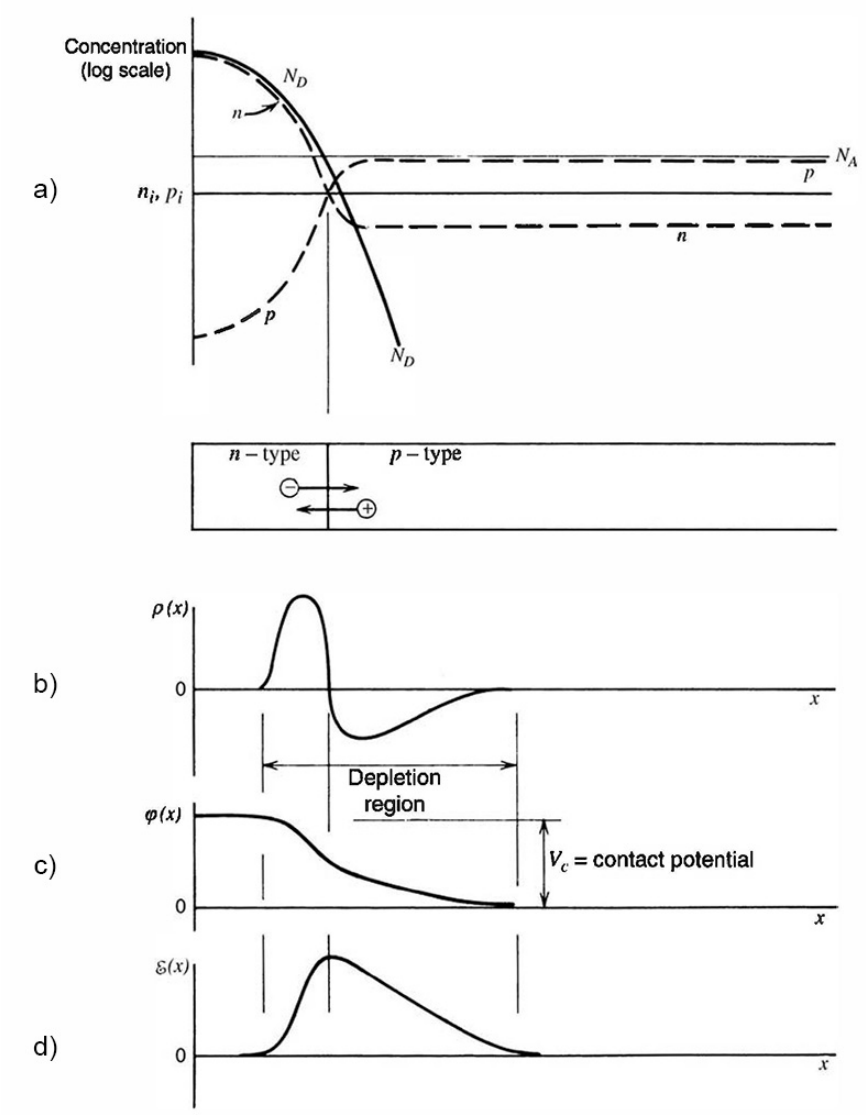

Figure 2.2: Example of dopant concentration profile for pn-junction formed by diffusing donor impurities into p-type semiconductor crystal is illustrated in a). Resulting space charge profile, electric potential and electric field after mobile charge carriers diffused across the junction are illustrated in b), c) and d), respectively [2].

Theory that follows is based on references [1, 2]. For known space charge distribution ρ, solving Poisson's equation:

$$\nabla^2\varphi = -\frac{\rho}{\epsilon}, \tag{2.1}$$

gives contact potential φ, that is the potential difference across the junction. ϵ is dielectric constant of the medium. Magnitude of the electric field can be found by taking gradient of the potential:

$$\vec{E} = -\vec{\nabla}\cdot\varphi. \tag{2.2}$$

Electric potential and electric field across the junction for space charge distribution of figure 2.2b are illustrated in figures 2.2c and d, respectively. In the last graph it is easy to see that electric field reaches its maximum at the point, where the transition from n- to p-type material takes place. This electric field sweeps any electrons created near the junction towards n-type side, and similarly all the holes towards p-type side. The concentration of mobile charges is thus greatly suppressed in the depletion region. The remaining immobile charges (ionized donor sites and filled acceptor sites) do not contribute to conductivity, so depletion region has very high resistivity compared to the n-type and the p-type materials on either side of the junction. As incident ionizing radiation creates electron-hole pairs in the depletion region, electric field attracts electrons and holes to opposite electrodes and their motion induces electrical signal. However, standard contact potential is around 1 V, which is not enough to collect all of the created charges. Reverse biasing the junction to enhance the natural potential difference allows charges to drift faster, which decreases the effect of trapping and recombination [2].

By using a simplified model we are able to derive some of the properties of reverse biased pn-junction. It is assumed that semiconductor wafer is thick enough so that depletion region does not reach either surface. Such detectors, where some portion of wafer thickness remains undepleted, are referred to as partially depleted. Otherwise, when depletion region spans through the whole wafer thickness, the detector is fully depleted. We elaborate only the case, where n-type side of the junction is more doped than p-type side and we approximate the fixed charge profile with uniform charge distribution, as shown in figure 2.3a:

$$\rho(x) = \begin{cases} eN_D & \textit{for } -x_n < x \leq 0 \\ -eN_A & \textit{for } 0 < x \leq x_p \end{cases} \tag{2.3}$$

An origin is set at the position of the junction, with x_n and x_p describing the length of the depletion region on n- and p-type side of the junction. Initially, the semiconductor starts as neutral, then the charges rearrange themselves to form depletion region. After the charge rearrangement, the net charge must remain zero. The following equation states this condition:

$$N_A x_p = N_D x_n. \tag{2.4}$$

By integrating Poisson's equation (2.1) for uniform charge distribution in one dimension from equation (2.3) and by applying boundary condition in which the electric field must vanish at both ends of the charge distribution (see figure 2.3b), we get an expression for electric field:

$$-E(x) = \frac{d\varphi}{dx} = \begin{cases} -\frac{eN_D}{\epsilon}(x + x_n) & \textit{for } -x_n < x \leq 0 \\ \frac{eN_A}{\epsilon}(x - x_p) & \textit{for } 0 < x \leq x_p \end{cases} \tag{2.5}$$

By integrating once again the expression above with reverse bias boundary condition, we get the electric potential in equation (2.6) and illustrated in figure 2.3c. This boundary condition states that the n-type side is biased with some external voltage V_{bias}, while the p-type side is held at zero voltage. The total potential difference is then V = V_{bias} + $V_{contact}$, but usually $V_{bias} \gg V_{contact}$ condition holds.

$$\varphi(x) = \begin{cases} -\frac{eN_D}{2\epsilon}(x + x_n)^2 + V & \textit{for } -x_n < x \leq 0 \\ \frac{eN_A}{2\epsilon}(x - x_p)^2 & \textit{for } 0 < x \leq x_p \end{cases} \tag{2.6}$$

Solutions for either side of the junction must match at $x = 0$. Combining this condition with request for charge neutrality in equation (2.4) makes it possible to obtain x_p and x_n. The total width of depletion region follows:

$$d = x_n + x_p = \sqrt{\frac{2\epsilon V}{e}\frac{N_A + N_D}{N_A N_D}}. \tag{2.7}$$

For specific case we are considering, when $N_A \ll N_D$, then equation (2.7) can be approximated to:

$$d \cong \sqrt{\frac{2\epsilon V}{eN_A}}. \tag{2.8}$$

The resistivity ρ of the doped semiconductor is given by

$$\rho_{n,p} = \frac{1}{e\mu_{e,h}N_{D,A}}, \tag{2.9}$$

where μ is mobility of the majority charge carrier. Inserting equation (2.9) into (2.8) gives:

$$d \cong \sqrt{2\epsilon V \mu_h \rho_p}. \tag{2.10}$$

Alternatively, if the n-type side was lightly doped and depletion region dominantly

extends to that side, in the expression above we would simply replace μ_h with μ_e and ρ_p with ρ_n.

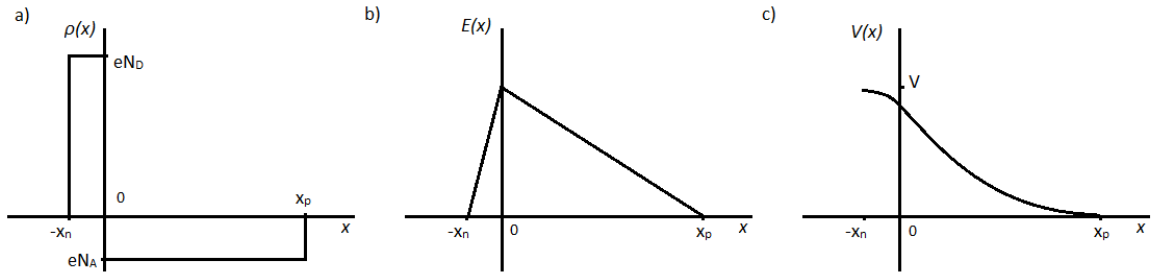

Figure 2.3: The electric field b) and potential c) derived from uniform space charge distribution shown in a).

From equation (2.10) is easy to see how applied voltage affects the width of depletion region. Since the depleted part of the semiconductor bulk is the only sensitive part of the detector, it is desirable to have largest depletion width possible. One limit is physical thickness of the wafer. Otherwise, for a given semiconductor sample, the depletion width increases with increasing bias voltage. It is advantageous to have semiconductor material with highest possible resistivity, because that way full depletion can be reached with lower voltages, as indicated in equation (2.10).

The maximum operating voltage for any diode detector must be kept below the breakdown voltage. If the reverse bias voltage exceeds this point, a sudden breakdown in the diode can occur and the reverse current would abruptly increase, often with destructive effects. Sudden increase of leakage current can be an indication of an imminent detector breakdown, so monitoring its values provides additional level of protection [1, 2].

2.2 Interaction of radiation with matter and generation of ehps

To truly understand the formation of electron-hole pairs in semiconductors we shall take a better look at the structure of their energy levels.

In an isolated atom, electrons occupy atomic orbitals. Each of the orbitals has a unique and discrete energy level. When two atoms interact, their atomic orbitals overlap. As a result, quantized atomic energy levels split into two molecular levels of different energies, stated by the Pauli exclusion principle, which dictates that no two electrons can occupy the same quantum state in a quantum system. The same

argument applies if a large number N of identical atoms are brought together to form a periodic crystal lattice. Following the Pauli principle, each atomic orbital now splits into N different discrete molecular orbitals. Since the number of atoms in a crystal is in the order of 10^{23} cm^{-3}, the newly formed molecular orbits are very closely spaced in energy. In fact, they are so close that they can be considered as a continuum, which we then call an energy band. Energy bands are separated by band gaps, regions with no available energy levels. Figure 2.4 shows forming of the bands as a function of the interatomic distance between silicon atoms with atomic energy levels E_1 and E_2. When the Si atoms finally form the crystal, they are settled in periodic lattice with equilibrium interatomic distance [14, 15].

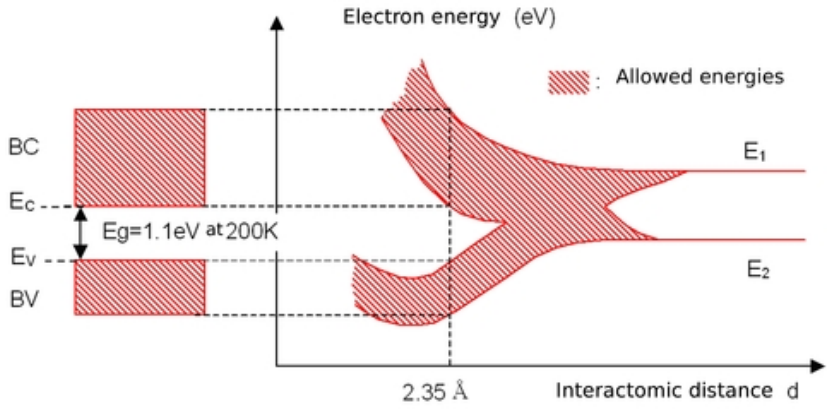

Figure 2.4: Formation of the energy bands for electrons as a function of interatomic distance between the atoms in a silicon crystal with a diamond-type lattice structure [14].

In a simplified picture, we only consider the bands of interest. Ignoring for now any thermal excitations, they can be described as follows: the highest filled energy levels form a valence band, then we have a band gap followed by a conduction band consisting of empty energy levels. The width of this band gap determines whether material would be an insulator, a conductor or a semiconductor. This is illustrated in figure 2.5. The width of the gap is determined by the lattice spacing between the atoms, and therefore is dependent on temperature and pressure [1].

Outer-shell electrons that are bound to specific lattice sites within the crystal, form the valence band. In silicon, these electrons are part of the covalent bonds that hold the crystal together. Electrons in the conduction band are free to move through the whole crystal. The number of electrons in a semiconductor crystal is just enough to fill all the available sites within the valence band, so without thermal excitations

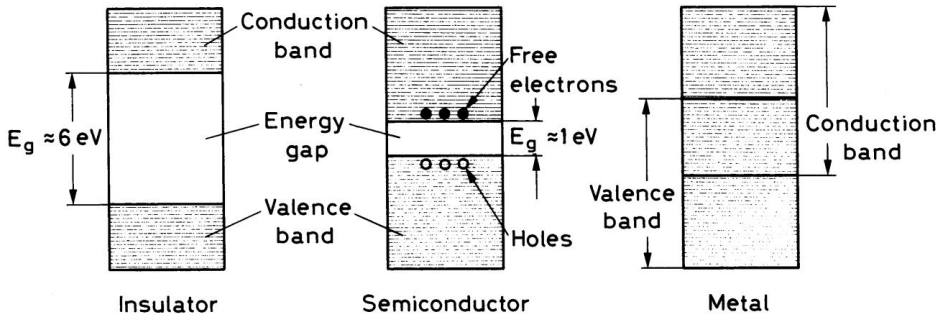

Figure 2.5: Energy band structure of insulators, semiconductors and conductors [1].

there would be no electrons that contribute to electrical conductivity of the material. However, thermal excitations are present at any nonzero temperature. Single excitation creates an electron in otherwise empty conduction band, and leaves a vacancy, called a hole, in the otherwise full valence band. Under the influence of electric field, the motion of both electrons and holes contributes to the observed current. Those electron-hole pairs are the main information carriers in semiconductor detectors.

Experimentally important quantity is the average energy spent by the primary charged particle to produce one electron-hole pair. This so called ionization energy is much smaller in semiconductor detectors than in other types of radiation detectors. From this follows that for the same deposited energy, semiconductor detector produces more charge carriers, which is beneficial for energy resolution [2].

Energy deposited by passing radiation depends on many parameters, such as type and energy of radiation or detector material.

2.2.1 Interactions of charged particles with matter

Stopping power of the material is described by quantum-mechanical semiempirical Bethe-Bloch equation. Its form differs slightly for heavy and light particles, latter referring to electrons and positrons. For heavy particles in the MeV energy range it is important to note the following part of Bethe-Bloch equation [1]:

$$-\left(\frac{dE}{dx}\right)_{collisions} \sim \frac{Z^2}{E}, \tag{2.11}$$

where Z is charge of incident particle in units of e, and E is its energy. Energy loss of heavy charged particles in matter is primarily the result of inelastic collisions with the atomic electrons. For particles with unit charge, ionization energy loss dominates

the energy range from few MeV to few GeV [16]. Energy loss of particles with unit charge in the beginning of this energy range is illustrated in figure 2.6 for several different materials. According to equation (2.11), the stopping power for silicon (Z_{Si}=14) would fall in between the curves for carbon (Z_C=6) and iron (Z_{Fe}=26). The energy loss is greatest for low-energy particles, according to functional dependance in equation (2.11). Characteristic drop in stopping power, clearly visible for all the materials in figure 2.6, corresponds to global minimum of the energy loss curve. Such particles are referred to as minimum ionising particles (MIPs). One characteristic of MIPs is homogeneous deposition of energy along its path through detector material. TCT measurement with infrared laser simulates the effect of MIP passing through the detector. At higher energies, energy loss starts to depend logarithmically on particle energy [1, 12].

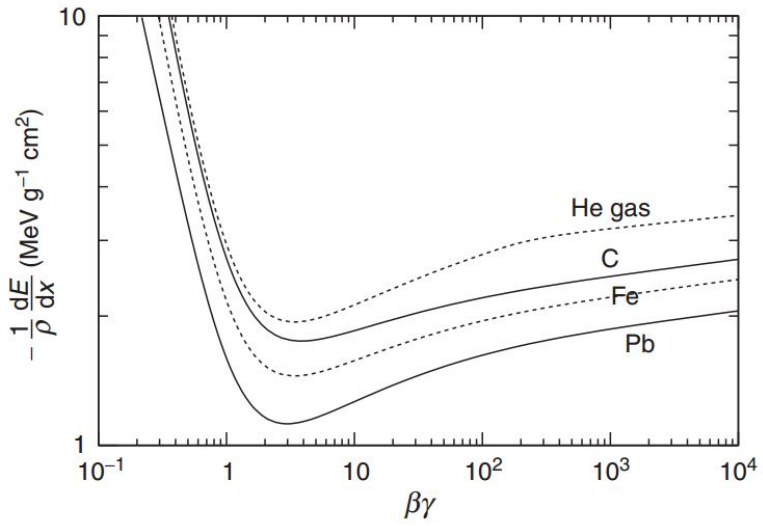

Figure 2.6: The ionisation energy loss curves for charged particles with $Z = 1$ traversing lead, iron, carbon and gaseous helium. The $\beta\gamma$ is equal to p/mc, where p is particle momentum and m is particle rest mass. Energy is related to momentum according to relativistic equation $E^2 = (pc)^2 + (mc^2)^2$ [12].

All charged particles lose energy through the ionisation of the medium in which they are propagating, but other energy-loss mechanisms may be present depending on the particle type. In MeV energy range, the ionization loss of electrons and positrons, depends linearly on Z and logarithmically on energy. In addition, bremsstrahlung can play an important role as well [1, 12]. Bremsstrahlung is the emission of electromagnetic radiation arising from scattering in the electric field of a

nucleus. The energy loss by electromagnetic radiation is approximately given by:

$$-\left(\frac{dE}{dx}\right)_{radiation} \sim E \cdot Z^2. \tag{2.12}$$

The bremsstrahlung emission probability is the inverse square function of the particle mass, so radiative energy loss has significant contribution only for the lightest charged particles, where at some critical energy radiation loss starts to dominate [1].

2.2.2 Interaction of photons with matter

The behaviour of photons in matter is drastically different from that of charged particles. Main interactions are photoelectric effect, Compton scattering and pair production. All of these interactions completely remove the photon from the incident beam, either by scattering or absorption. As a consequence, photon beam is attenuated in intensity, but remaining photons energies are unchanged. Cross sections of these three processes are much smaller compared to inelastic electron collisions, which results in X-ray and gamma radiation being much more penetrating than charged particles.

In the photoelectric effect a photon is absorbed by the atomic electron. As a result, the electron is unbound from the atom. The energy of the ejected photoelectron is equal to the energy of the absorbed photon reduced by the value of the electron binding energy. Due to momentum conservation, only bound electrons can participate in photoelectric effect, because then the nucleus can absorb the recoil momentum. Cross section for photoelectric effect is given by [2]:

$$\sigma_{photo} \propto \frac{Z^n}{E_\gamma^{3.5}}. \tag{2.13}$$

Dependence on the atomic number Z varies somewhat with the energy of the photon (i.e. $Z^{n(E)}$). At MeV energies, this dependence goes as Z to the fourth or fifth power [1, 8]. Specific curve for photon absorption in silicon is plotted in red in figure 2.7.

Pair production is possible if photon energy exceeds 1.022 MeV/c^2, which is equal to the rest energy of electron-positron pair. In the field of a nucleus, a photon is converted to an electron and a positron. Photon must be near a nucleus for pair production, in order to satisfy conservation of momentum [1]. Cross section for this

process depends on Z of the material as [2]:

$$\sigma_{pair} \propto Z^2. \tag{2.14}$$

In figure 2.7 corresponding curve for photon absorption in silicon due to pair production is plotted in light blue [11].

Combined effect of pair production by high-energy photons and bremsstrahlung emission by high-energy electrons is the formation of electron-photon showers, or cascades [1].

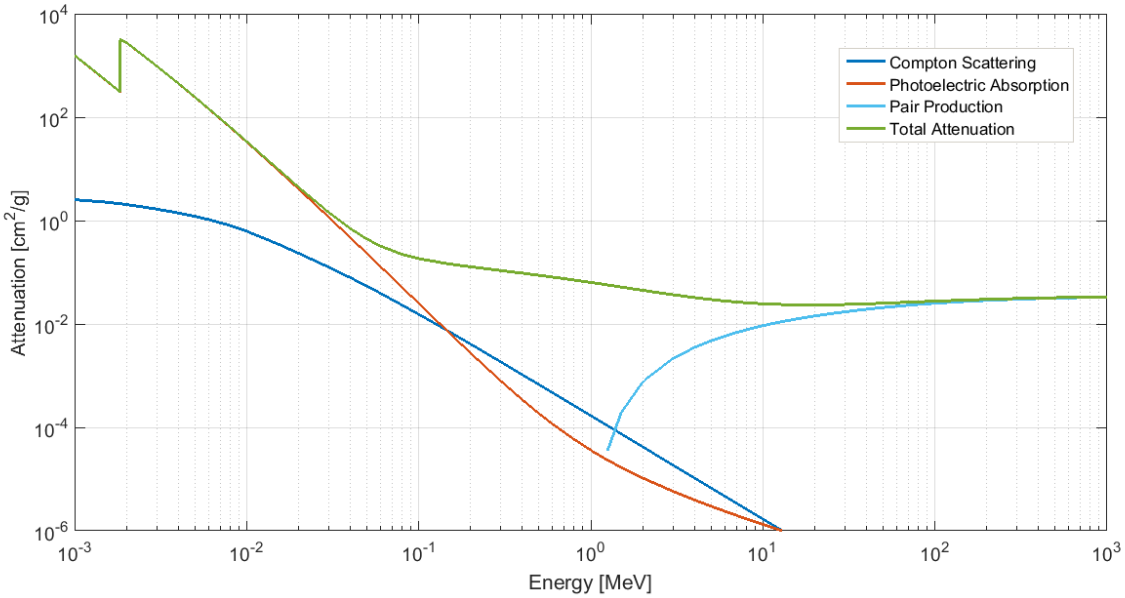

Figure 2.7: X-ray absorption in silicon, as a result of the three main interaction processes. Plotted with data from NIST XCOM: Photon Cross Sections Database [11].

Pair production and photoeffect are especially suitable for spectroscopy applications, because photons pass all of their energy to charged particles, which are considerably easier to detect.

Compton scattering, on the other hand, describes scattering of photons on free electrons, as it is illustrated in figure 2.8. If photon energy is much higher than the binding energy of electrons in atoms, they can also be considered as essentially free [1]. Cross section for Compton scattering depends on the material as [2]:

$$\sigma_{Compton} \propto Z. \tag{2.15}$$

In figure 2.7 photon absorption in silicon due to Compton scattering is plotted in

dark blue.

The total probability for photon interaction in matter is given as a sum of all the mentioned contributions and typical interaction diagram for silicon detector is presented in figure 2.7 with green curve. Alternatively, using Planck hypothesis, $E = hc/\lambda$ photon energies can be converted to corresponding wavelengths.

Electron-hole excitation is one of the possible outcomes of ionizing energy transfer. Incident radiation interacts with matter in many ways, as we have just discussed in detail. Ionizing energy loss, as well as interactions that result in most, if not all of the incident particle energy being transferred to charged particles are beneficial for the number of generated ehps.

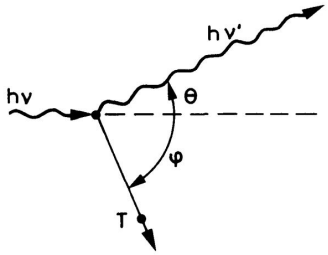

Figure 2.8: Illustration of Compton scattering [1].

2.3 Effects of radiation on silicon detectors

The electron-hole pair generation is fully reversible process that leaves no damage. On the other hand, the non-ionizing energy transfers to the atoms of the crystal lead to irreversible changes [2]. Surface and bulk damage are two types of radiation damage in silicon detectors. While surface damage can be minimized with proper optimization of detector processing, bulk damage is unavoidable after high irradiation doses. Incident radiation above some specific energy can displace atoms from their lattice sites. This generates vacancy-interstitial pairs, or Frenkel pairs. If enough energy is transferred in the initial collision to the so-called primary knock-on atom, it can create a new Frenkel pair [13]. Around 25 eV is needed to dislodge Si atom from its lattice site [2]. Photons require energies above 250 keV in order to cause displacement damage in the collision with Si atoms. X-rays therefore do not produce displacement damage. Gamma rays can cause displacement damage also via Compton electrons [6]. Protons and neutrons interact with matter more readily, so even

low-energy particles can generate Frenkel pairs. The minimum kinetic energy of neutrons needed to cross the threshold is around 180 eV. Threshold for fast electrons is more than thousand times higher, at around 260 keV, due to much smaller mass [2].

Neutrons create defect clusters with defect concentrations as high as 10^{19} cm^{-3}, while gamma irradiation creates point like defects uniformly distributed in the detector bulk. Proton irradiation produces effect between neutron and gamma irradiation, with both clusters and single defects produced in Si bulk [9]. Since the main characteristics of semiconductors arise from their crystalline structure, it is expected that displacement damage will have certain macroscopic consequences. Vacancies and interstitials are mobile. Some will recombine shortly after they are created, but others may diffuse apart and combine with other defects and impurities, creating more complex defects. The defect complexes create electrical states in the silicon band gap. Depending on the position of these levels, there are three possible effects: increase in leakage current, evolution of effective doping concentration and degradation of charge collection efficiency [5]. Increase in deep energy levels near the middle of the band gap promotes hole emission from valence band to defect state and also electron emission from defect state to conduction band. The increased generation current leads to an increase in overall reverse bias leakage current. It has been found experimentally that the leakage current increases linearly with 1 MeV neutron equivalent fluence Φ_{eq} [13]:

$$I_{leakage} = \alpha \cdot V \cdot \Phi_{eq}. \tag{2.16}$$

Proportionality constant α is called the current-related damage rate, while V is the active volume of the detector. The leakage current depends strongly on temperature:

$$\frac{I_{leakage}(T_2)}{I_{leakage}(T_1)} = \left(\frac{T_2}{T_1}\right)^2 e^{-\frac{E}{2k}\left(\frac{T_1 - T_2}{T_1 T_2}\right)}, \tag{2.17}$$

with E being the the band gap energy and k the Boltzmann constant. Large leakage current can damage a detector, so heavily irradiated detectors often have to be operated at reduced temperatures. Deep energy levels near the middle of the band gap can also act as recombination centers, when combined effect of electron capture from conduction band and hole capture from valence band results in recombination. This leads to charge loss. Trapping centers are shallow levels near the edges of the band gap that temporarily capture charges. If detrapping time is long compared to

the charge collection time, this also adds to the charge loss effect. The charge collection efficiency (CCE) defined as ratio of collected charge after and before irradiation therefore decreases with the accumulated radiation damage. All of the mentioned emission and capture processes are illustrated in figure 2.9 [5, 6].

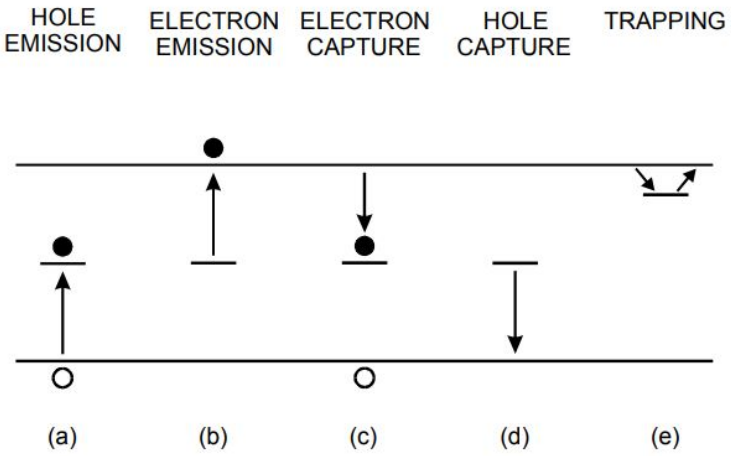

Figure 2.9: Emission (a and b), capture (c and d) and trapping (e) processes of electrons and holes in defect states [6].

Third macroscopic effect is linked to removal of existing dopants from their active sites and the creation of new charged defect states near the band edges, which changes the effective doping concentration. Depending on the specific processes involved, this can either increase or decrease the required operating voltage [5, 6]. Specific case, when radiation damage introduces electrically active defects of opposite type (acceptor levels in donor-dominated bulk), effective doping concentration gradually decreases, until space charge sign inversion (SCSI) occurs. Following this, depleted detector bulk transitions from n- to p-type [2]. This is often called type inversion.

2.4 Approaches for improving radiation hardness

As mentioned in the introduction, several approaches for increasing radiation hardness have been established.

Material engineering is deliberate modification of the detector bulk material. It includes defect engineering, where impurities are added to silicon in order to affect the formation of electrically active defect centers. Another area of research is the use of other semiconductor materials, such as silicon carbide (SiC), diamond or cad-

mium telluride (CdTe). One of the most successful examples for defect engineering of silicon is oxygen-enrichment [4]. It was found that oxygen in silicon captures vacancies, forming vacancy-oxygen complexes, which are in general less harmful to detector operation [5].

The two most common silicon wafer development methods are Czochralski (Cz) growth and Float Zone (FZ) Crystal technique. Silicon detectors have traditionally been processed using Float Zone silicon (FZ-Si) wafers. In FZ method a polysilicon rod is brought into contact with a seed crystal. The rod is then locally melted with radio frequency (RF) heating. The RF heater, and with it the melted zone, moves along the rod. FZ-Si crystals are grown without quartz crucibles which are a common source of impurities. The resulting silicon is of high purity and high resistivity. Due to high resistivity, the detector can be fully depleted at reasonable operating voltages. However, FZ-Si has a low oxygen concentration [17, 18].

Nowadays, the Czochralski crystal growth method enables the production of silicon wafers with sufficiently high resistivity and with well-controlled oxygen concentration. During the Czochralski growth method, the silicon melt is held just a few degrees above the melting point and a single crystal seed is slowly pulled up from the molten silicon, thus developing an ingot. The slow retraction allows the melt to solidify in perfect crystal orientation at the boundary. The oxygen dissolves into the melt during the process, enriching the final crystal homogeneously with oxygen [17–19]. Cz-Si has high oxygen content in order of 10^{17}-10^{18} cm^{-3} [3]. Since the silicon melt is electrically conductive liquid, magnetic field can be used for better control of mechanical perturbations and oscillations in the melt. This allows more precise control of the desired oxygen and dopant concentration dissolving from the crucible [20]. This is important when one wants to make very homogeneous (in terms of doping and oxygen concentration) Si wafers from center to edge. Application of magnetic field during the crystal growth is a special case of the Czochralski technology. Silicon produced this way is called magnetic Czochralski silicon (MCz-Si) [19].

Example of a silicon ingot, from which wafers are later cut, is shown in figure 2.10b. The benefit of using oxygen-enriched silicon for radiation detectors is in slower change of effective doping concentration, when detector is irradiated with charged hadrons [5]. Gamma irradiation generates net positive space charge in materials with high oxygen concentration, such as MCz-Si. On the other hand, in

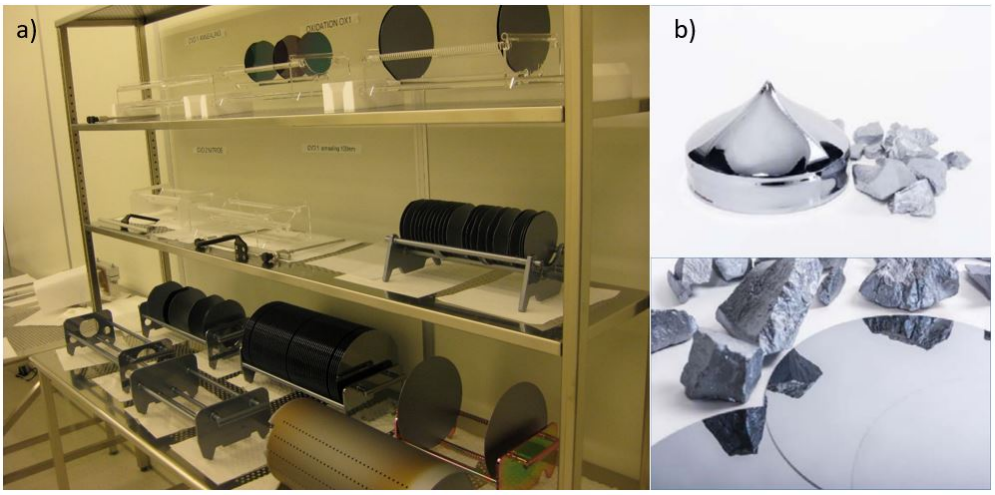

Figure 2.10: The pictures show: a) Si wafers in a clean room; b) poly-Si fragments with beginning of silicon ingot (top) and with polished wafers (bottom); [photographs courtesy of J. Härkönen and Okmetic Ltd.]

standard FZ-Si gamma irradiation generates negative space charge. It was found that generation of negative or positive space charge has a clear dependence on the oxygen concentration [5, 9].

The oxygen concentration does not affect leakage current and trapping increases with irradiation dose. Furthermore, oxygen does not help with radiation damage from neutron irradiation, since local defect concentration in generated defect clusters exceeds the oxygen concentration of the silicon bulk [5].

Besides material engineering, variations of detector operational conditions are also studied. This includes for example effects of cooling or operation in current injected mode.

Finally, device engineering studies possible improvements in radiation hardness by modifying detector structure. That includes modification of the electrode configuration, thinning of the detector bulk, using p-type materials and developing 3D detectors [3].

Most commonly used diode layout designs for segmented detectors in high-energy physics include strip and pixel detectors. Close-up photographs of both are shown in figure 2.11. In the beginning of the 2000s, standard strip detectors consisted of p-strips implanted into a lightly doped n-type substrate ($p^+/n^-/n^+$, p-in-n or n-type detectors). After SCSI occurs, the maximum of the electric field is on the side opposite to the read-out strips, which results in reduced charge collection at low voltages. The CCE can be improved by using p-type detectors (n-in-p, $n^+/p^-/p^+$) [21]. The

CERN Research and Development Collaboration that focuses on radiation hard semiconductor devices for very high-luminosity colliders (or RD50 for short) proposed using Czochralski silicon (Cz-Si or MCz-Si) and p-type sensor structure. The p-type detectors do not suffer from SCSI, so the electric field remains on the segmented side of the sensor. This leads to signal being dominantly generated by electrons. Since electron mobility in Si (μ_e(300 K) = 1350 cm^2/V·s) is about three times higher than that of the holes (μ_h(300 K) = 480 cm^2/V·s) [2], the trapping during charge carrier drift is reduced. All of this enables higher CCE in p-type detectors [3, 20]. The drawback of p-type diodes is the more complex fabrication.

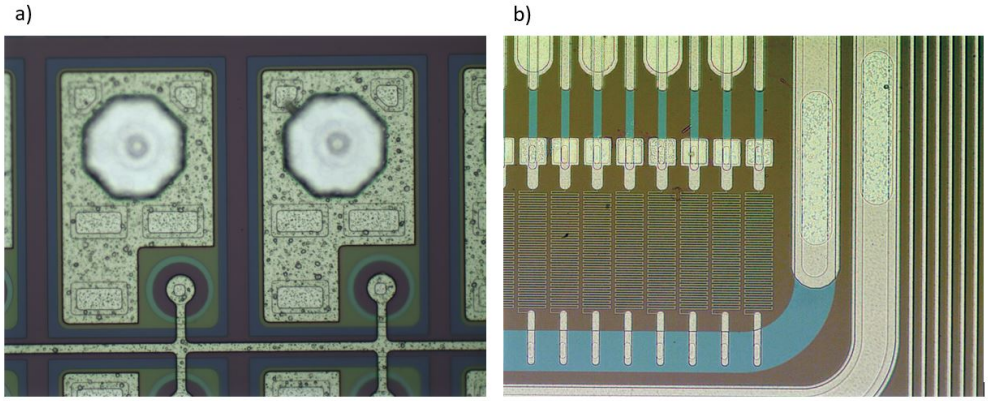

Figure 2.11: Photographs show: a) CMS pixels; b) strip detector. The CMS pixel dimension is 120μm x 150μm and strip width is 20μm. [photographs courtesy of J. Härkönen]

Work that follows will focus on silicon pad diodes with non-segmented electrodes. Pad detector is simplified test structure of a real detector that measures particle tracks. Example of pad detectors studied for this thesis is shown in figure 3.1.

3 Si detectors used in this study

3.1 Pad detector layout

The silicon detectors used in this study are pad detectors processed for research purposes at Micronova Nanofabrication Centre in collaboration with Helsinki Institute of Physics. The main structure of the pad detector can be divided into active area and guard rings. High voltage is usually applied at the back contact, and signal is read out from the grounded front contact [5], as it is shown in simplified scheme of figure 3.1a. Composite photograph of one of the used samples is in figure 3.1b.

With this biasing configuration, leakage current is flowing through the bulk of the detector from back to front contact. In DC-coupled devices the induced signal goes directly to the preamplifier, together with any leakage current present which is detrimental for signal-to-noise ratio (SNR). The details of signal formation due to induction will be studied in detail in the following chapter. For now, it is clear that reducing the leakage current is imperative for optimizing detector operation. One way to do that is by cooling the detector, since leakage current depends exponentially on temperature, as stated in equation (2.17). Using AC-coupling is another available approach [5, 17]. In TCT measurements DC diode is connected to a discrete component called Bias-T, which effectively makes AC-coupling. Inside of the Bias-T device are the bias-R and coupling capacitor [37].

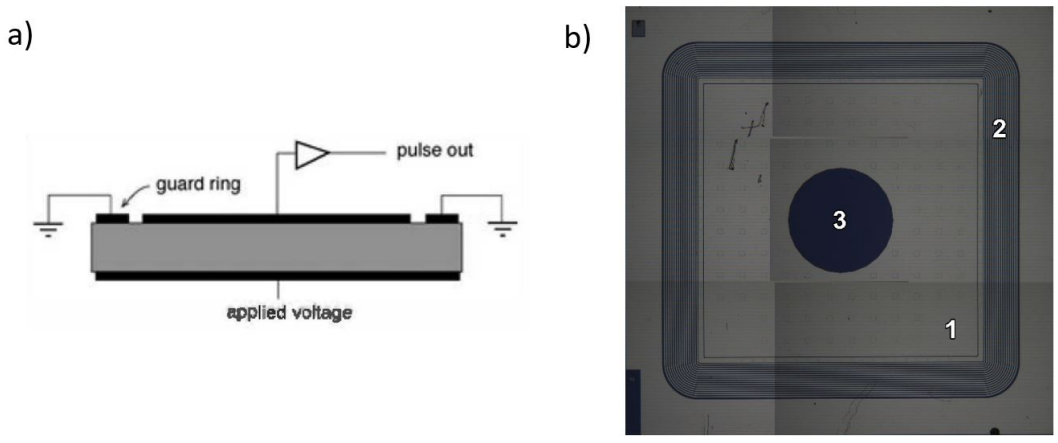

Figure 3.1: a) Pad detector configuration shows grounded guard ring structure that protects the readout electrode. Bias voltage is applied to the back side electrode [2]. b) Front side of the n-type pad detector with non-segmented electrode (1), guard ring structure (2) and optical opening (3) for TCT characterization. The picture was composed from six close-up photographs.

Additionally, specific parts of the detector layout all have their purpose in advancing the operation of the detector.

Guard rings (GR) shape the field inside the sensitive area to minimize edge effects. There are two basic connection schemes. In configurations with single guard ring structure, GR is grounded and thus provides a drain for the leakage current from the edge of the detector. The second configuration uses one or more floating guard rings which offer stepwise drop in voltage from outside in. This can help to avoid electrical breakdown. Combinations of grounded and floating guard rings are also possible [2, 5, 17].

Incorporating guard rings into detector structure reduces slightly the area of the readout electrode which by itself would reduce detector efficiency. However, it also excludes from the active area the edge regions where trapping can be more severe due to cracks and dangling bonds, since both introduce additional energy levels in the forbidden gap [2].

Since pad detectors in figure 3.1b are intended for research testing, in the center of the front electrode an opening is made to enable penetration of laser light for TCT method. The opening is hence termed optical.

3.2 Detector processing

There are many different variations of detector processing developed by companies and research groups during the years. For relatively simple pad detectors main steps are oxidation, ion implantation, metallisation of the electrodes and passivation.

Fabrication process generally begins with high-resistivity mirror-like polished silicon wafers that are mildly n- or p-type [2].

Surface of the wafers is oxidized by an atmosphere of O_2, H_2O steam or N_2O. Layer of silicon dioxide SiO_2 that is formed serves as a hard mask for ion implantation.

Patterning of SiO_2 by first mask defines n^+ and p^+ areas.

Next step is doping of both sides with appropriate ions. Usual dopants are phosphorus n-type Si, and boron for p-type. By driving in the dopants, the goal is to change effective doping concentration in selected regions of the surface [22]. Ion implantation is done by bombarding the wafer with an ion beam. Ions will be stopped in the semiconductor bulk in the regions opened in the preceding steps. Average pen-

etration depth depends on ion beam energy, which is usually fixed to be 70 keV for phosphorous and 30 keV for boron (as phosphorous is heavier ion). In regions where SiO_2 is still present, ions will be stopped in this insulating layer, unless their energy is high enough to penetrate into the semiconductor [22]. Wafers can be placed on a rotating disk to guarantee a homogeneous implantation [17].

After ion implantation silicon dioxide is completely removed from the surface by hydrofluoric acid (HF).

Second stage of the processing is electrical passivation by the means of a homogeneous field insulator. For that purpose n-type wafers are oxidized again. Silicon oxide provides good passivation of the silicon surface, because most of the open bonds are saturated by the oxide in the Si-SiO_2 region. After oxidation only small amount of dangling bonds are left, roughly around 10^{11} cm^{-2}. Reduced concentration of surface states reduces surface leakage current. Oxidation is performed at temperatures above 1000 °C, which is usually the highest temperature process. High temperature results in oxygen diffusing through the layers of oxide already grown so they can react with silicon at the Si-SiO_2 boundary [22]. Heat treatment simultaneously helps with several other important processes. Since ion implantation results in very shallow impurity profile, temperature treatment is needed to stimulate diffusion which drives impurities further into the silicon volume. Furthermore, deposition of the ion impurities in the crystal is not sufficient to obtain desired electrical properties. Heat treatment brings the ions into regular lattice positions (drive-in), which is a necessary condition for their activation in the desired fashion [22,23]. Result is forming of the pn-junction at desired depth and with desired diffusion profile. Heat treatment can also thoroughly anneal the substantial damage of the crystal lattice caused by the ion implantation [5, 17, 22].

In p-type detector processing the approach to electrical passivation is different. Positive oxide charge of the dielectric layer on the detector is attracting electrons to silicon-oxide interface, which can short-circuit the segmented areas. Widespread methods for suppressing this accumulation are p-spray and p-stop techniques. The p-spray provides positive space charge near the surface, which compensates the electron accumulation. The p-stop method introduces localized implants that block conductive paths the accumulating electrons are forming. Both methods introduce addi-

tional steps to detector processing which leads to higher production cost. In addition, the p-stops and the p-sprays might introduce localized high electric fields, which increase the likelihood of early breakdowns [20]. Recent studies proposed an alternative to commonly adopted p-stop or p-spray technologies with SiO_2 field insulator. Instead of growing an oxide layer all over the detector, thin film of Al_2O_3 is grown with Atomic Layer Deposition (ALD) technique on top of the silicon wafer after the ion implantation and prior to the metallisation. The Al_2O_3 field insulator introduces negative oxide charge and thus accumulates holes instead of electrons.

The ALD is based on successive, separated and self-terminating reactions of reactants called precursors with substrate surface [24, 25]. In each reaction there are sites for only one monolayer to bond with the original surface. Temperature of the silicon substrate is the primary controlling parameter. Since ALD is based on surface-gas reactions, their self-limited nature allows excellent thickness control [26, 27].

Wafers with homogeneous insulator are patterned by second mask that defines the contact openings through the insulator.

Next step is metallisation, which provides thin ohmic electrical contacts at the front and rear surfaces. Aluminium is standard metal in Si radiation detector applications, due to its good electrical conductivity, easy shaping and good connectivity to silicon. Back side is usually fully metallised, while the front side must be patterned after aluminium deposition using third mask to define electrodes [2, 5, 17].

Final step of metallisation procedure is again thermal treatment, which is required for producing a good electrical and mechanical contact between the silicon and the aluminium. This is called aluminium sintering [22].

At this stage, relatively simple wafer of diode detectors is usually ready for dicing. Mechanical and chemical passivation is not necessary for diodes intended for use in lab measurements. Detectors for particle tracking systems, on the other hand, are additionally passivated for protection since they undergo many bonding, testing and module assembly procedures.

Passivation of metal electrodes has to be made at temperatures below the ones required for aluminum sintering (350-450 °C). Thus, low temperature oxide and nitride deposition method must be used. Usually it is Plasma Enhanced Chemical Vapor Deposition (PE-CVD) or ALD. Contact openings for probing and bonding through the

passivating insulator are opened by fourth mask. In order for contact to reach the metal, layer of SiO_2, Si_3N_4 or Al_2O_3 are wet etched.

Simplified illustration of the production sequence described so far is shown in figure 3.2.

Example of finished strip and pad detector wafers can be seen in figure 3.3.

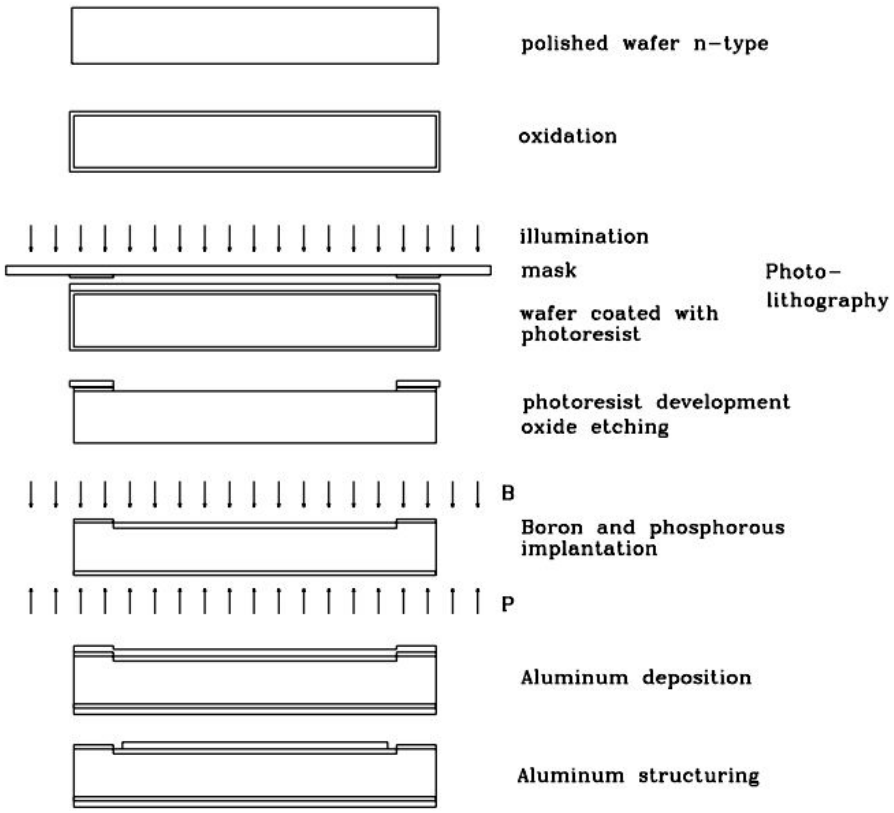

Figure 3.2: Simplified production sequence of a pn-junction pad detector [22].

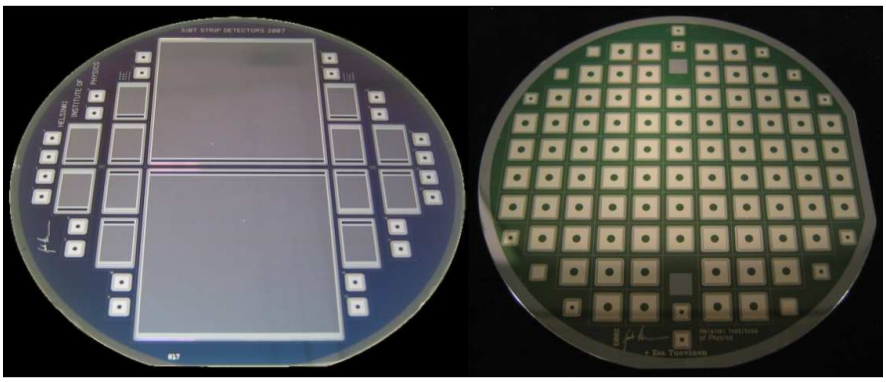

Figure 3.3: Example of finished wafers with strip detectors and pad detectors with optical openings intended for testing [5].

4 Transient Current Technique (TCT) method

The Transient Current Technique is the measurement of time-resolved current pulse shapes in semiconductor detectors, induced by laser light pulses of subnanosecond duration. Laser light excites non-equilibrium holes and electrons which then drift through depleted region of the detector bulk. Their movement induces current pulses on the electrodes until they are collected there. During their drift, charge carriers might be trapped by radiation induced defects [3, 28, 29].

When infrared laser (IRL) is used (λ = 1064 nm), ehps are homogeneously generated through the entire 300 μm silicon bulk. Thus, IRL TCT measurement is a way to simulate the signal created by minimum ionizing particles. The measured current transient is generated by both electrons and holes [3, 19].

The 660 nm red laser (RL) is another wavelength used in TCT measurements in the course of this work. The red laser penetration depth is shallow, around 3 μm [31]. In p-type detectors with $n^+/p^-/p^+$ configuration front-side (n^+) illumination results in current pulse dominantly induced by holes, because holes have to drift through the entire thickness of silicon in order to be collected at negatively biased p^+ electrode. Electrons drift only a few μm to reach the grounded n^+ electrode. They are collected so fast that the resulting small signal is damped by the rise-time of measurement electronics. If p-type detector is illuminated from the back side (p^+) electrode, current would arise mainly from electron drift. The process in n-type detectors with $p^+/n^-/n^+$ configuration is analogue to what is previously described for p-type detectors [3, 28].

The p- and the n-type diodes used have round optical opening in Al metallisation. Thus, RL TCT measurement of n-type detectors observes currents dominantly induced by the motion of electrons, and in p-type detectors by the motion of holes.

By analyzing the current transients, it is possible to extract the full depletion voltage, the effective trapping time and the CCE, as well as the electric field distribution and the sign of the space charge in the bulk (and thus detect whether SCSI has happened) [9, 28, 30].

All of this makes the TCT a powerful tool for sensor characterization before and after irradiation [9].

4.1 The Shockley-Ramo theorem for induced currents

The output pulse begins to form immediately after the charge carriers start their motion towards the electrodes. Once the last of the carriers arrive at their collecting electrodes, the process of charge induction ends and the pulse is fully developed [2].

It is prudent to mention that the varying voltage on the electrodes also causes current to flow in the external circuit in order to accommodate amount of charge on the electrodes as dictated by the relation $Q = C \cdot V$ [32]. However, if we disregard fluctuations in bias voltage, the induced charge is independent of the value of the applied potential on the electrodes [34].

Shockley-Ramo theorem states that instantaneous current received by the given electrode due to the motion of a single electron is given by:

$$i = q \cdot \vec{v} \cdot \vec{E_0}, \tag{4.1}$$

where $\vec{v}$ is the velocity of the charge carrier, q is its charge and $\vec{E_0}$ is the so called weighting field. The weighting field is the electric field, which would exist at the instantaneous position of a charge carrier under the following circumstances: the charge carrier is removed, the electrode of interest is raised to unit potential and all other conductors are grounded [2, 33].

Outline of the derivation of the general expression given above follows the reasoning of original articles by Shockley and Ramo ([32] and [33]). It is presented in Appendix D.

To find the weighting potential V_0 one must solve the Laplace equation, $\nabla^2 V_0 = 0,$ for the geometry of the detector with artificial boundary conditions outlined in the derivation in Appendix D. Weighting field can be obtained from $\vec{E_0} = -\vec{\nabla} \cdot V_0$. It is also necessary to determine the actual electric field, because generated charge carriers follow the electric field lines. If the charge velocity is proportional to the electric field in the space charge region, then the position of the charge as a function of the time can be uniquely determined. All of this makes possible to determine the shape of the induced pulse in dependance on time. The amplitude of the induced charge is independent of the depth at which the charge carriers are generated, provided they are all collected [2].

4.2 Determining the detector characteristics from the TCT data

Before starting to mathematically manipulate the obtained data, a look at the shape of the TCT voltage can give us qualitative measure of the electric field distribution in the detector bulk, as well as the sign of the space charge. Recalling the Shockley-Ramo theorem in equation (D.5), we set $q = e \cdot N_{e,h}(t)$ for the aggregation of laser induced drifting charges. Here e is the unit charge and $N_{e,h}(t)$ is number of drifting electrons and holes. The number of charge carriers has exponential dependance on time due to trapping:

$$N_{e,h}(t) = N_{e,h}(t_0)e^{-\frac{t-t_0}{\tau_{eff}^{e,h}}}. \tag{4.2}$$

The carrier injection time (start of the laser pulse) is denoted by t_0 [35]. We can assume that the charge velocity has a simple linear dependance on the electric field in the bulk $E(x)$, and the constant of proportionality is the charge mobility μ. Diode detectors have parallel plate electrodes, so the weighting field is simply $E_0 = 1/w$, where w is detector thickness. Considering all of this, we have:

$$I_{e,h}(t) = \frac{e}{w} \cdot N_{e,h}(t_0)e^{-\frac{t-t_0}{\tau_{eff}^{e,h}}} \cdot \mu_{e,h}E(x). \tag{4.3}$$

As described in Chapter 2, the electric field has a maximum at the region where the pn-junction takes place. Equation (4.3) now implies that regions with stronger electric field yield higher induced current [3]. Current increases as charge drifts from low field to high field, and then decreases again as it passes the maximum and drifts towards the lower field on the opposite side [9]. If the RL TCT illumination is on the same side as the collecting junction, a descending transient signal is measured. If it is on the opposite side, an ascending signal is measured [5]. The RL TCT measurement therefore serves as a quick qualitative check of the electric field distribution in the detector bulk, which is important for CCE as having high field near the collecting electrode can help reduce trapping effects [19]. Since the electric field is determined by space charge distribution, switch in the high field side indicates that SCSI has taken place [9].

Integration of the IRL TCT signal provides a measure of the collected charge from

passing of a minimum ionizing particle:

$$i_{TCT} = \frac{V_{TCT}}{R_{osc}} = \frac{dQ}{dt} \Rightarrow Q \propto \int V_{TCT} dt', \tag{4.4}$$

where R_{osc} is input resistance of the oscilloscope [3]. This is typically 50 Ω. The integrated signal is not divided by the resistance for simplicity, so charge is in arbitrary units.

In unirradiated detector the charge collection increases with increasing the thickness of the depletion region and saturates at voltages above V_{fd}, provided the current integration time is longer than the time charges need to reach the collecting electrodes [35].

The full depletion voltage V_{fd} is determined from the integral of the transient signals plotted as collected charge vs. voltage. Linear fits are made for voltages below and above approximate value of V_{fd}. The crossing point of the two fits is taken to be full depletion voltage.

When measuring heavily irradiated samples, part of the drifting charge is trapped at radiation-induced defects. The effective trapping time τ_{eff} is a statistical time constant which describes how long electrons or holes are able to drift before getting trapped. Inverse of the trapping time is the effective trapping probability. If charge is not released in time to still be collected, it is lost from the signal [3]. At voltages above the full depletion, further increase of the field increases the drift velocity. This reduces the overall drift time of the charges and by that also the amount of charges being trapped. If the integration time for developing the signal is long enough, all the trapped charges are detrapped and the total collected charge again saturates at voltages above V_{fd}. This is seldom the case, so special approach was developed in order to correct the obtained data and compensate for lost charges. It is called Charge Correction Method (CCM) [35]. However, this particular technique is beyond the scope of this work.

The total collected charge Q_{coll} is given by the integral in equation (4.4) and it depends on the thickness of the depletion region. Trapping is governed by the exponential law, according to equation (4.2). We can write CCE to be the product of the electric field related geometrical term (CCE$_g$) and the trapping related exponential term (CCE$_t$). Geometrical term is simply d/w, where d is thickness of the depletion

region and w is detector thickness. At voltages above the full depletion, the CCE_g is 100 $\%$. Then the CCE_t can be deduced by integrating the induced current in equation (4.3). Setting the charge injection time $t_0 = 0$ and defining t_{dr} to be the drift time of the charges, collected charge in the presence of trapping is obtained. Integrating again without the exponential term gives the amount of charge that would be collected, if the trapping were completely absent. The ratio of these two values gives gives CCE_t and the total CCE follows [3, 36]:

$$CCE = CCE_g \cdot CCE_t = \frac{d}{w} \cdot \frac{\tau_{eff}}{t_{dr}} \left(1 - e^{-\frac{t_{dr}}{\tau_{eff}}}\right). \tag{4.5}$$

4.3 Technical description of the TCT setup

The TCT setup at the PaRaDeSEC laboratory at IRB consists of two diode lasers (red with λ = 660 nm and infrared with λ = 1064 nm) that provide simultaneously external trigger signal for data acquisition oscilloscope. There are also laser power supply, DC voltage supply filter and Bias-T all enclosed in a metal box, which protects detector from light sources other than laser light during the measurement. The TCT setup at RBI is provided by Slovenian company Particulars. There is also a 3-axis translation mount with a XY-plane that holds a heat remover (with provided cooling liquid inlets), a Peltier cooling element and an iron mounting plate. The sample holder has a small magnet on its back so it can be fixed on the mounting plate. A photograph of the mounting system is shown in figure 4.1. The Peltier element was not used in measurements described in this work. However, the heat removing system combined with Julabo F250 chiller was necessary to lower the leakage current in the irradiated samples.

Laser pulses were transmitted to the sample detector via an optical fibre connected to a small objective. The Z-direction of the 3-axial translation mount was used to adjust the focus of the laser. Pulse length was in the order of tens of picoseconds.

Keithley 2410 1100V SourceMeter unit (SMU) provides bias voltage to the back side of the detector. Any high frequency distortions of the power supply that would affect the measured signal are filtered out with DC high voltage filter. Filtered high voltage is then connected to the Bias-T and finally to the back of the detector [37].

Connecting the sample to the bias circuit was realized by placing it on a copper

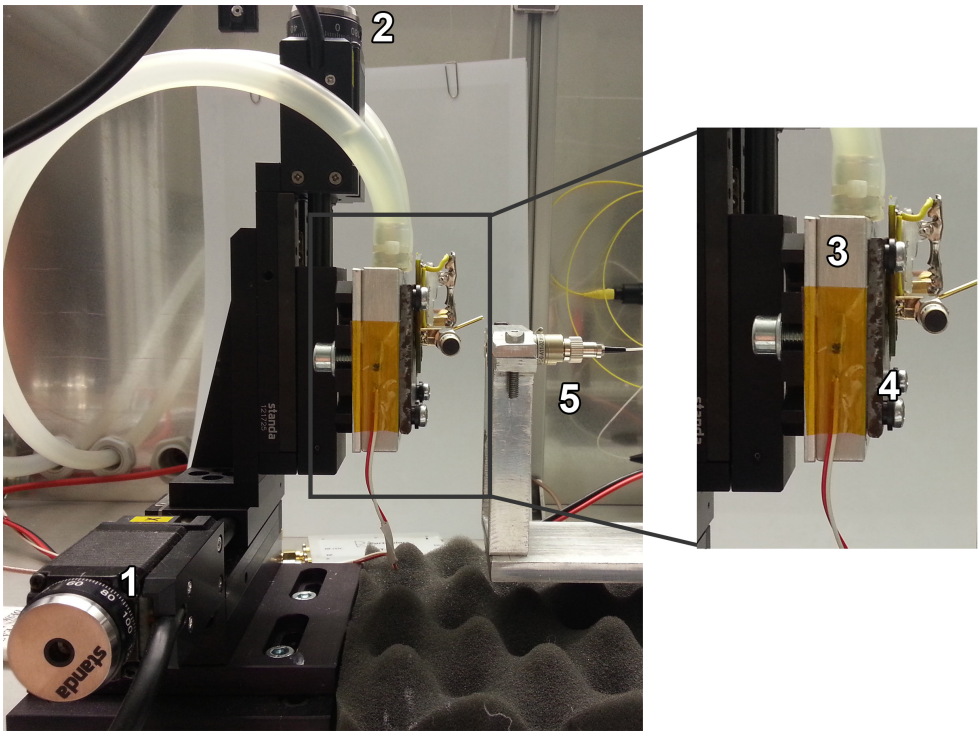

Figure 4.1: TCT setup: (1) and (2) X-Y translation system, (3) Heat remover with Peltier element and cooling liquid inlets, Pt-1000 for temperature monitoring is taped on the side, (4) Iron mounting plate with sample holder prepared for measurement, (5) Objective with connected optical fibre which transmits laser pulses.

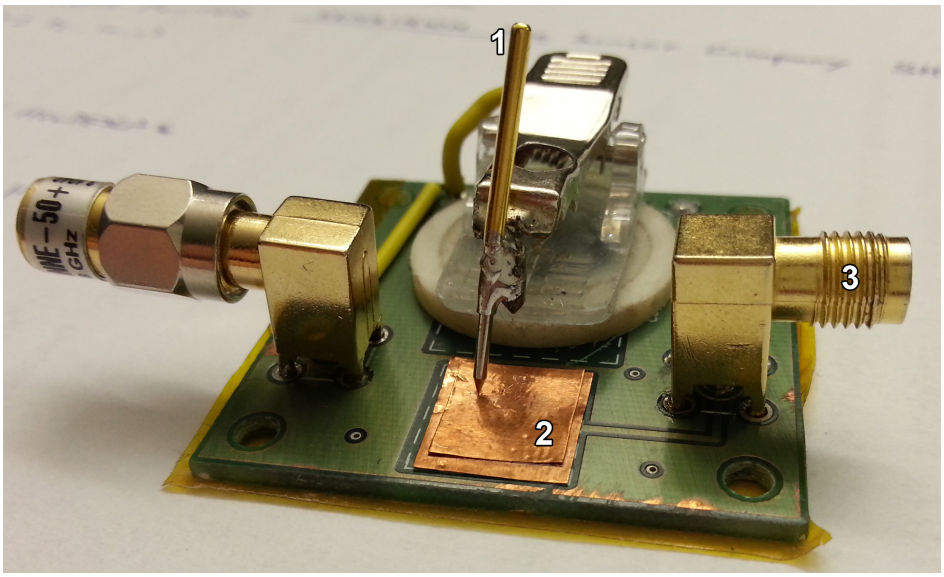

Figure 4.2: Sample holder: (1) Conductive needle holds sample in place, (2) Copper plate provides electrical connection to the back side of the detector, (3) Input for Lemo cable (readout and biasing).

plate and fixing its position with a conductive sample holder needle. This can be seen in figure 4.2. Same cable, used for biasing the copper plate, was used to read out the induced signal. The Bias-T was then used to decouple the high-voltage biasing

from the low-voltage contribution of the induced current [37]. The signal from the detector was then conducted into Channel 1 of the Teledyne LeCroy WaveRunner 8404M-MS oscilloscope. Laser trigger was connected on Channel 2.

The laser trigger rate at all measurements in Si was kept at 200Hz, which is typical event rate per cm^2 in high-energy physics experiments. The laser was connected to PC via USB cable, which enables manual control over certain parameters. The oscilloscope was also connected to the PC and a data acquisition software was used to read and store the current pulses as .txt files. Matlab and QtiPlot software were used for plotting and analysis of the obtained data.

A complete schematics of the TCT setup is shown in figure 4.3. The TCT laser system is illustrated in figure 4.4.

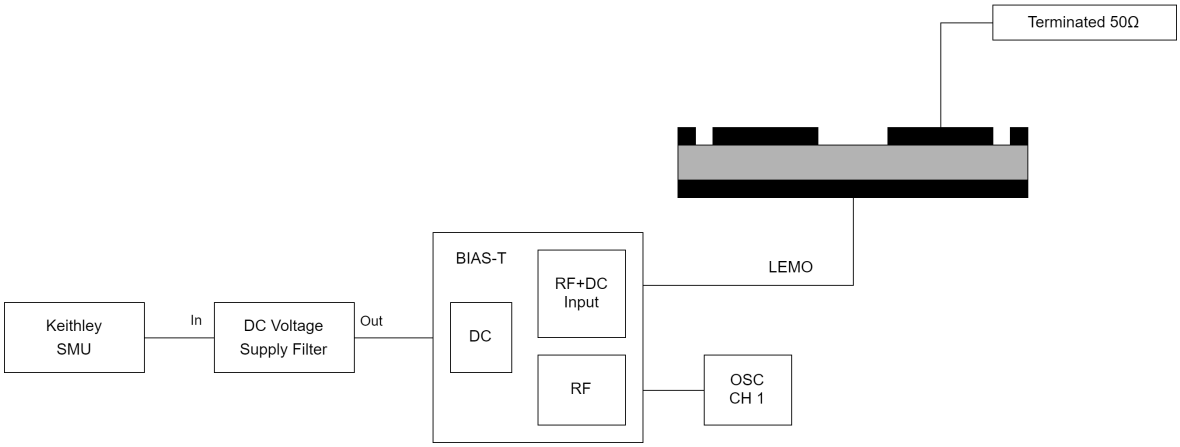

Figure 4.3: Scheme of the TCT measurement setup. The laser pulses are aimed at the center of the optical opening on the front side electrode.

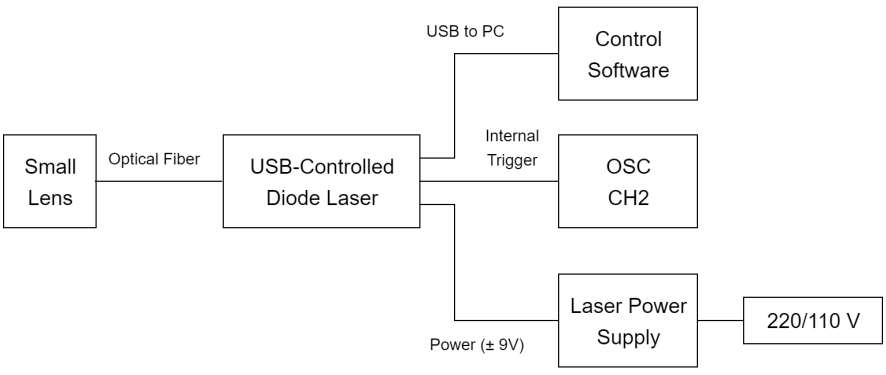

Figure 4.4: Scheme of the TCT laser system.

The total leakage current of the circuit was monitored with Keithley SMU with current compliance limit set to 105 μA. Samples irradiated with high doses require cooling in order to reduce the leakage current and allow voltage scan on higher bias

values. The chiller circulated a cooling liquid through the system and cooled the iron mounting plate. Layer of thermal paste was used between sample holder and the iron plate to improve heat transfer.

During the measurements, temperature and humidity were monitored in roughly 10 min intervals with Sensirion Smart Gadget SHT21 humidity sensor placed inside the TCT setup. This sensor gives information about the humidity, the temperature and the dew point inside the TCT box. The temperature was additionally measured at the base of the heat remover and on the sample holder itself. For this, two Pt-1000 thermometers were used.

5 ^{60}Co irradiation

5.1 Decay scheme

In a β^- decay an electron and an electron antineutrino are emitted from the nucleus as a result of the transformation of a neutron into a proton:

$$n \rightarrow p + \beta^- + \bar{\nu_e}. \tag{5.1}$$

The atomic number of the decaying nucleus is therefore increased by one unit, but the mass number remains the same [1].

^{60}Co is synthetic radioactive isotope with half-life of 5.27 years. It decays by β^- decay to excited levels of the stable isotope ^{60}Ni. The decay scheme is presented in figure 5.1. In most cases (99.925 %) ^{60}Co decays to 2.5057 MeV energy level of ^{60}Ni. The first gamma ray with energy 1.1732 MeV (99.9 %) is emitted when nickel atom transitions to excited state with lower energy. The second gamma ray with 1.3325 MeV energy (99.982 %) is emitted in transition to stable ground state. The values in parenthesis are probabilities of the corresponding transition [1, 41].

The energies of both gamma rays are too small to trigger a thermonuclear reaction. Thermonuclear reaction or photodisintegration would include high-energy gamma ray exciting the nucleus which would then immediately decay by emitting a subatomic particle. Since the ^{60}Co irradiation is most often used for radiotherapy and variety of sterilization applications, it is of utmost importance that irradiated material does not become radioactive itself [38, 39, 41]. ^{60}Co gamma rays fall into energy range, where the Compton scattering dominates the energy loss processes in silicon, which is to say between 0.15 and 1.5 MeV (see figure 2.7). The Compton electrons cause displacement damage [6].

5.2 Doses and dosimetry

The activity of the source is defined as the mean number of decays it undergoes per unit time. It depends on the amount of source material, so greater sample means greater total number of decays. There are several units for activity, but the one recommended today is Becquerel (Bq) due to its simple definition where 1 Bq = 1

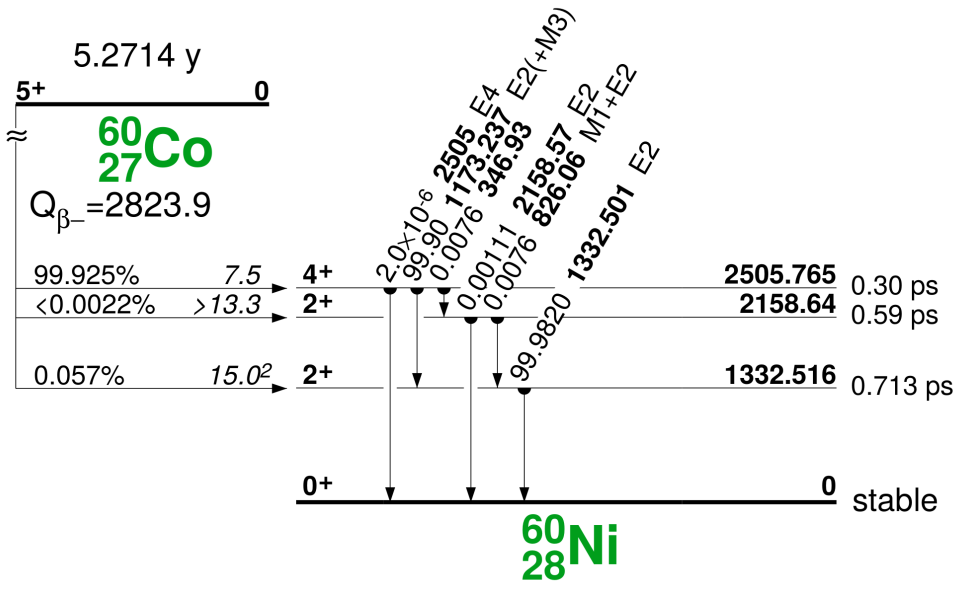

Figure 5.1: Basic decay scheme of ^{60}Co [41].

disintegration/s [1].

Absorbed dose measures the total energy absorbed per unit mass. The unit of measurement is 1 Gray (Gy) = 1 Joule/kg [1]. In practise the dose is calculated from time period the sample is irradiated and from experimentally measured dose rate. The dose rate can be measured by ionization chamber or passive dosimeter, depending on the expected dose rate and the constraints of the irradiation setup. The obtained data is then used to predict a dose rate in subsequent time period, according to the exponential decay law.

At RBI there is a panoramic ^{60}Co gamma irradiation facility. The radioactive source is contained along the axis of a high upright cylinder. Such configuration allows isotropic irradiation in the area around it. The dose rate decreases as inverse square of the distance from the cylinder axis. The samples can also be put inside the cylinder, where dose rate is much higher, approximately around 9 Gy/s. For comparison, lethal dose for humans is around 10 Gy, if administered to the whole body [40].

On days irradiation of the samples took place, source activity was 2.55 PBq. Out of 8 samples in total (4 n-types and 4 p-types), one n- and one p-type sample were not irradiated. The rest were positioned at 40 cm from the central axis of the ^{60}Co source. The irradiation took three days in total. Every day one n- and one p-type detector were taken out. The absorbed doses for irradiated detectors are shown in

table 5.1. In the analysis that follows the non-irradiated samples will be referred to as Sample 1. The detectors irradiated for one, two and three days are called Sample 2, 3 and 4. It will always be clearly noted whether n- or p-type detector is being considered. The approximate 1 MeV neutron equivalent (n_{eq}) doses are calculated using the conversion 1 Gy $\cong 3{\cdot}10^9$ cm^{-2} [6]. After irradiation, the samples were kept in a fridge at -23 °C to prevent annealing of radiation damage.

	Day 1	Day 2	Day 3	Total Dose	1 MeV n_{eq} dose
Sample 1 (n33, p8)	-	-	-	0	0
Sample 2 (n12, p3)	60.102	-	-	60.102	$1.80{\cdot}10^{14}$
Sample 3 (n26, p7)	60.102	62.461	-	122.563	$3.68{\cdot}10^{14}$
Sample 4 (n21, p6)	60.102	62.461	64.187	186.750	$5.60{\cdot}10^{14}$

Table 5.1: The absorbed doses in kGy for n- and p-type detector samples after ^{60}Co gamma irradiation are shown in columns 2-4. The last column contains approximate 1 MeV neutron equivalent doses in units of n_{eq}/cm^2.

6 Measurements and results

Three TCT measurement conditions (with IRL and RL illumination) were applied for both n- and p-type samples. Abbreviations are introduced for simplicity: M1 - measurements before irradiation of Samples 2-4, M2 - room temperature (RT) measurements after irradiation of Samples 2-4, M3 - measurements after irradiation of Samples 2-4 with chiller (approximately 10 °C below RT). In all three measurement sets, the non-irradiated Sample 1 was measured again as a reference.

RL TCT voltage scan of n-type samples

A front-side illumination of n-type samples with red laser results in electron-dominated transient current, as was discussed earlier in section 4.2. The TCT voltage scan for 25, 100, 250 and 500 V are presented in figure 6.1 for Sample 3, and the rest are in the Appendix A. From descending shapes of the pulses for all n-type samples both before and after irradiation, we can conclude that pn-junction (and with that the maximum of the electric field) remains at the front side. That means the bulk stays n-type even after the highest irradiation dose of almost 200 kGy, i.e. no SCSI was observed.

The duration of the pulse directly corresponds to the drift time of the electrons from the point of their creation to their collection at the electrodes. Significant trapping of the charge carriers would have observable effect on the pulse duration. If the irradiation doses applied to detectors had introduced significant trapping, signal pulses would be considerably shorter. The drift time for electrons extracted from pulse widths at 250 V are around 17, 19 and 19 ns for M1, M2 and M3 measurement conditions, respectively. There was no significant change in pulse duration between M1 and M2 measurements for irradiated samples, as it is clear from observation of the plots in figures A.1-A.4. This is the indication that CCE is still close to 100%.

Prior to M3 measurement, the TCT laser trigger changed due to an unknown problem, which resulted in almost 2 ns earlier triggering. The obtained signals shifted in time compared to earlier measurements, which makes data harder to read when put on the same plot. For more clarity, M3 measurements are presented in different color and with thinner line.

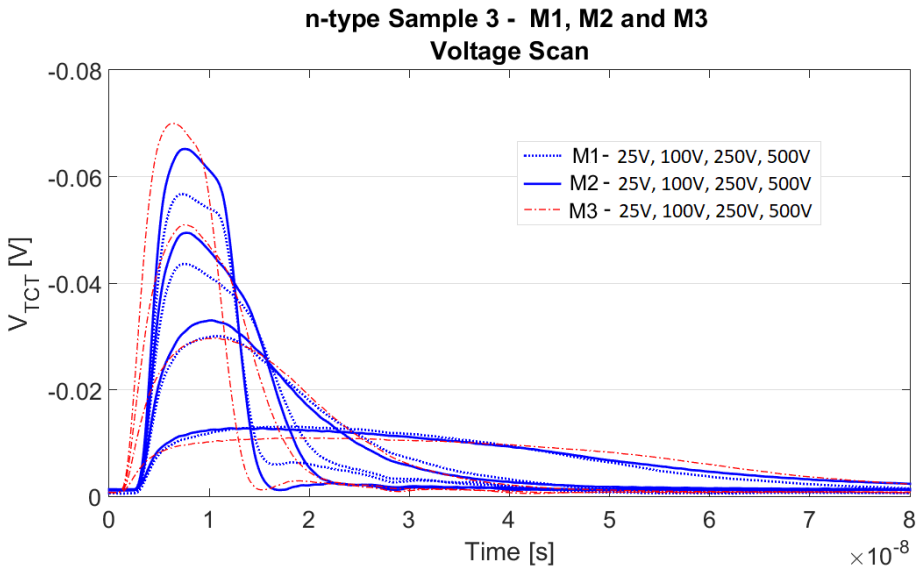

Figure 6.1: TCT voltage scan with red laser at 25, 100, 250 and 500 V. The plot presents signals from n-type Sample 3 obtained in M1, M2 and M3 measurement conditions.

All differences in pulse width were within experiment error of the TCT method.

RL TCT voltage scan of p-type samples

For p-type samples, red laser illumination of the front side results in hole-dominated current. From p-type detector configuration ($n^+/p^-/p^+$), it would be expected that collecting pn-junction with maximum of the electric field lies near the front side, at least in unirradiated detectors. The TCT voltage scans of p-type samples are presented in figure 6.2 for Sample 3 and the rest are in the Appendix B. The x-axis of all p-type plots shows absolute value of the voltage, since for p-type detectors biasing is negative. Contrary to expectation, pulse shapes indicate that pn-junction is on the back-side. The holes moving from n^+-side to p^+-side drift from low field to high field, as the current increases with time. However, slope is relatively small, which indicates that the detectors are just over the SCSI point [9]. This general shape is retained even after irradiation and can be noticed in all three sets of measurement conditions. It is possible that an error in production sequence caused introduction of thermal donors, which can lower the effective doping in p-type detectors.

Due to much higher leakage current in p-type samples, in comparison to the n-type ones, signals showed occasional jumps in the amplitude even with stable con-

stant biasing. That can be one of the signs of early detector breakdown. High leakage current prevented voltage scan of the high end of the intended voltage range. The M3 measurements, performed at approximately 10 °C lower temperature, allowed reaching few tens of volts higher bias values.

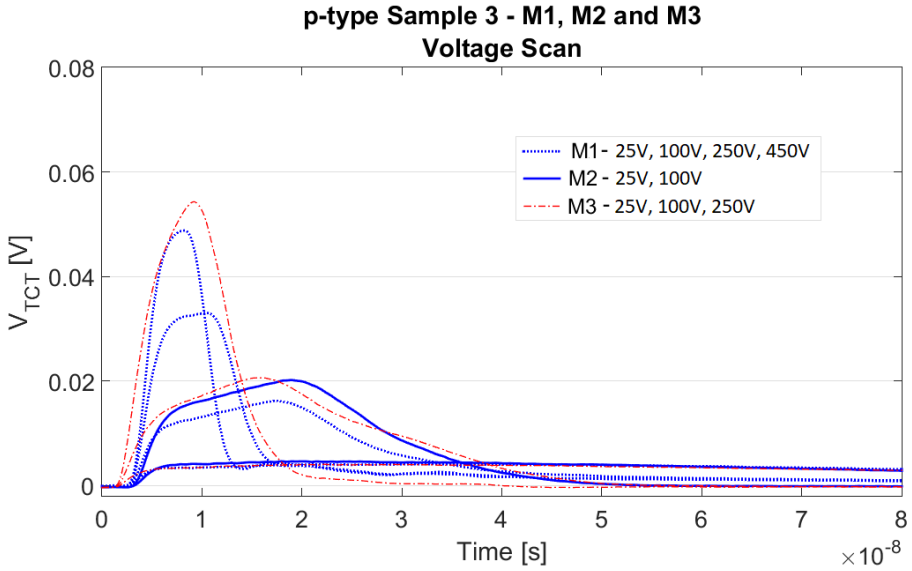

Figure 6.2: TCT voltage scan with red laser at 25, 100, 250 and 450 V. Plot presents signals from the p-type Sample 3 obtained in M1, M2 and M3 measurement conditions.

At 250 V, the detectors were well above full depletion voltage, and charges are collected within 14 to 17 ns in M1 measurement set, in around 17 ns in M2 measurement and for M3 measurement it took around 19 ns.

The signals at 25 and 100 V were very similar for all samples in all of the three measurements. It should be noted that for Sample 1, the M1 signal amplitude was approximately 20 mV lower than the M2 amplitude at 250 V (see figure B.1). Since this was non-irradiated sample, nothing changed in between these two sets of measurements in the detector itself. This change should be attributed to difference in the TCT experiment on different measuring days. However, the TCT signal for M3 at 250 V agrees with the signal obtained during M2 at 250 V. Taking Sample 1 as a reference, a comparison between M2 and M3 measurement sets can be made for the other samples as well.

In Sample 2, the amplitude of the pulse from M3 measurement gives 6 mV higher value compared to M2 signal at 250 V. This is an indication that some trapping is present, which was reduced by the cooling of the sample.

Samples 3 and 4 did not reach 250 V in M2 measurement, so the same effect

cannot be confirmed for higher irradiation doses.

Other than the changes in the amplitude in M3 measurements, there was no apparent change in the duration of the pulses due to cooling of the samples.

Apart from slight difference in signal amplitude in M2 and M3 measurements, no significant pulse change occurred due to irradiation of the detectors, same as was observed in consideration of n-type samples.

6.1 Determination of full depletion voltage

The measure of charge collection from a single minimum ionizing particle is obtained by integrating the transient pulses from TCT measurements with infrared laser over the whole recorded time range (980 ns, initiated by the laser trigger).

As discussed in Chapter 4, in the absence of trapping charge collection depends only on the thickness of the depletion region. From equation (2.9) we have seen that its thickness increases with a square root of the applied voltage. At the point of full depletion, limited by the thickness of the detector wafer (300 μm), the CCE$_g$ is at its maximum. Further increase of the applied voltage has no effect on the efficiency of the charge collection and the integrated charge saturates. An example of the described behaviour is shown in figure 6.3 for the collected charge in M1 measurement of the n-type Sample 3. Besides the total collected charge Q_{tot}, given by the integration of the full recorded pulse, the plot also shows the Q_{FWHM}. That is charge contained within full width at half maximum of the pulse. In this case, part of the collected charge is not taken into consideration. How significant that amount is, depends on the rise and the fall times of the pulse. The Q_{FWHM} curve rises more slowly, which makes the starting point of the saturation less evident.

For this reason, Q_{tot} was preferred for the determination of the full depletion voltage. However, integration of the whole pulse makes the resulting values much more sensitive to noise levels. Since the leakage current adds to noise, in the irradiated p-type samples Q_{tot} data was badly distorted and in some cases saturation point could not be identified at all. In this case, despite slow saturation, the Q_{FWHM} data was much more convenient for analysis. Slower rise time of Q_{FWHM} values gave up to several tens of volts higher V_{fd} estimation. For all n-type samples the Q_total data was

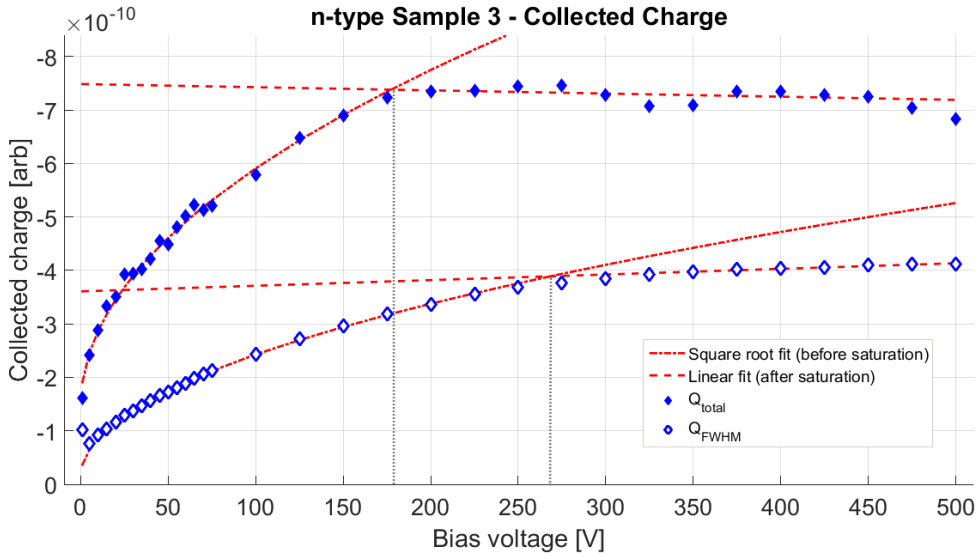

Figure 6.3: The plot shows the collected charge contained in the total pulse (Q_{total}) and within FWHM of the pulse peak (Q_{FWHM}). A square root function was fitted on the data before saturation, and linear fit was applied to the data after saturation. Since the FWHM integration causes some charge loss, saturation was slower and the point of full depletion was artificially higher. The plot presents data from Sample 3 M1 measurement.

used, and for p-type samples V_{fd} was determined from Q_{FWHM}.

Several different approaches were tried in effort to find the most accurate determination of full depletion voltage.

First idea was to automatise the V_{fd} determination via Matlab code to eliminate a possible introduction of a systematic error. However, varying behaviour of the charge collection in different measurements made it hard to fully automatise the process. The saturation was not always completely constant, and it was observed that rising slope before saturation can change angle up to three times. Semiautomatic process was then chosen, in which voltage range for linear fit was manually entered and the code then made linear fits to find the crossing point of the two lines. However, the Q curve shapes differ between the measurements and consistent choice of the proper voltage range was difficult to determine manually. Using this method, numerical results showed spread in V_{fd} values that simply is not visible in charge-voltage plots. Figure 6.4 shows Q-V plot of all n-type samples for all the measurements. While the Q-V plots for each of the measurements of p-type samples are presented separately in the Appendix C, since the Q_{FWHM} values obtained in different measurements overlap.

The best approach turned out to be completely manual determination from charge-

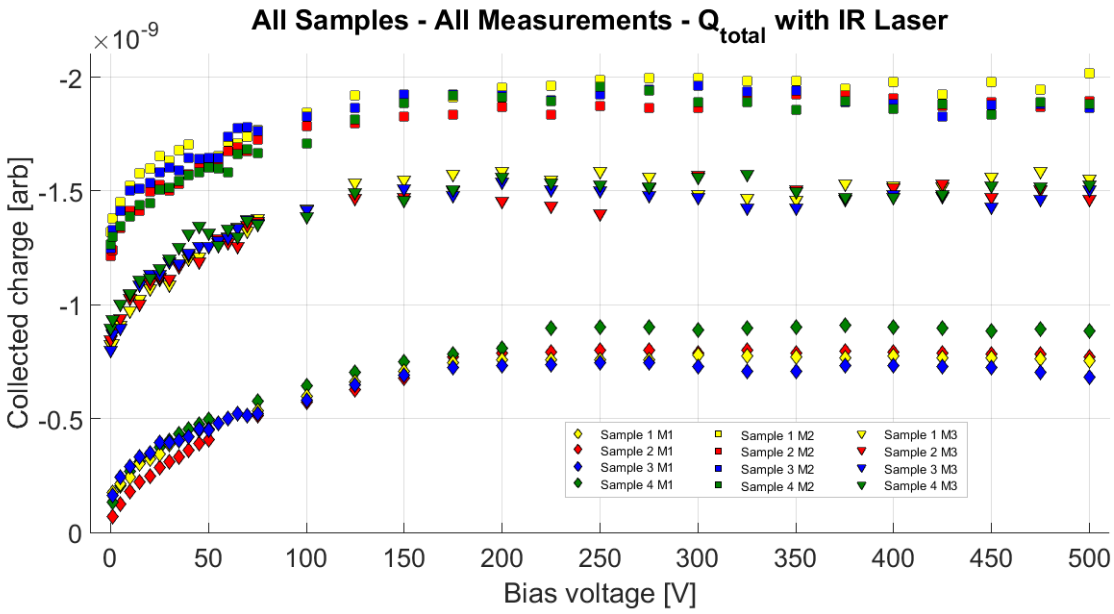

Figure 6.4: Charge-voltage plot shows the integrated total charge curves for all the samples and all of the measurements. It is clearly visible how the data for all the samples falls closely together within the same measurement set.

voltage plots using Matlab. The logarithmic scale was used to accentuate the change between rising and saturating behaviour. The lines were then drawn through data points before and after saturation point and the full depletion voltage was considered to be at the data point closest to the cross-section of the two lines. In most cases, the change was so sharp that the full depletion voltage could be determined within one (n-type) or three (p-type) data points. From this, we can estimate the standard deviation of the obtained results. For n-types samples, the full depletion occurred above 100 V for all detectors. In that range, the used voltage step was 25 V, so this can be taken as measurement error. In p-type detectors the full depletion happened at much lower values, mainly under 75 V, and in that range voltage step was 5 V. This gave a standard deviation of 15 V (for 3 data points).

Full depletion voltages determined by the last described method are presented in table 6.1 for n-type samples and in table 6.2 for p-type samples. An illustration of this process is shown in figure 6.5.

A comparison of the results from the same measurements (while keeping in mind general differences in measurements indicated by Sample 1 results) gives no indication of V_{fd} evolution with irradiation dose. The same conclusion can be confirmed by observing the charge-voltage plot with all samples from all measurements showed at once (see figure 6.4 for n-type and figures C.1-C.3 for p-type). Besides the differences

n-type	Sample 1	Sample 2	Sample 3	Sample 4
M1	175 V	175 V	175 V	225 V
M2	125 V	100 V	125 V	150 V
M3	125 V	125 V	125 V	125 V

Table 6.1: The full depletion voltage of n-type samples with a standard deviation of 25V for all of the presented results.

p-type	Sample 1	Sample 2	Sample 3	Sample 4
M1	50 V	25 V	30 V	60 V
M2	60 V	35 V	50 V	75 V
M3	75 V	100 V	75 V	75 V

Table 6.2: The full depletion voltage of p-type samples with a standard deviation of 25 V for Sample 2 in M3 measurement, and 15 V for the rest.

in the measurements themselves, the curves of the collected charge for all samples fall closely together, even after irradiation. In the non-irradiated samples this was expected, as all p-type and all n-type detectors came from the same production batch, which means they should have similar properties. In the irradiated samples on the other hand, this was further proof of radiation hardness of the used detectors under applied irradiation doses.

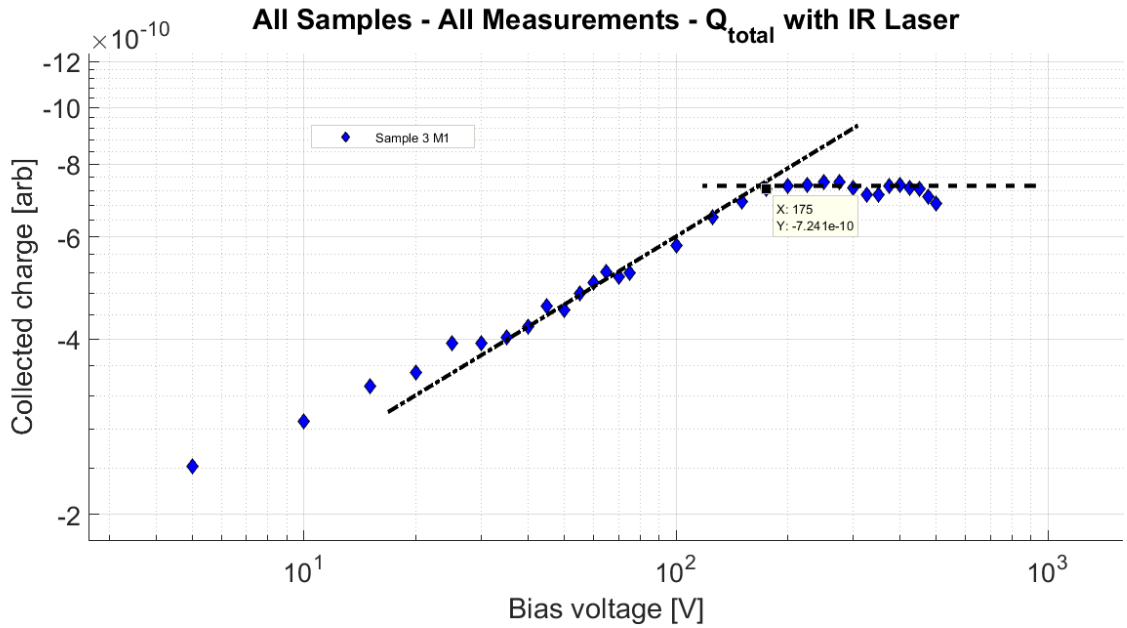

Figure 6.5: Determination of the full depletion voltage by accentuating the change using a logarithmic scale. N-type Sample 3 from M1 measurement is used as an example.

6.2 Evolution of the leakage current

It was already mentioned in equation (2.16) of section 2.3 that leakage current increases linearly with the fluence. If the volume of the detector is constant, we can fit the experimental data to linear function $I_{leak}(\Phi) = A \cdot \Phi + B$. To avoid possible underdepletion, the leakage current values were read out at values safely above the full depletion voltage. For the p-type detector chosen voltage was 100 V, while for the n-types the voltage was 200 V. Results of the linear fit are presented in figure 6.6 for n-type and in figure 6.7 for p-type samples. The black data points represent the leakage current of samples 2-4 in M2 measurement set, while the red data points are the same for M3 measurement.

For p-type detectors, the M2 measurement at RT showed rapid increase in leakage current. Samples 2 and 3 had higher leakage currents to begin with (0.504 μA and 0.082 μA, respectively) in comparison to Samples 1 and 4 (0.031 μA and 0.034 μA, respectively). This reflected in the M2 measurements, so the linear fit gave A(M2)$\approx$0. Cooling reduced the leakage current and the data readout voltage at 100 V was far enough from the breakdown point for linear dependance to become visible. Slope value gave $A(M3) = (1.2 \pm 0.1) \cdot 10^{-19}$ A cm^2. For M3 measurements, the results of the linear fit are given in figure 6.7 marked in red. The RT leakage current (M2) is marked in black on the same plot.

The leakage current at 200 V for n-type samples shows clear linearity in both M2 and M3 measurements. Same function was used for the linear fitting of the data, as for the p-type detectors described above. Figure 6.6 shows both sets of data along with linear fits. Again, M2 is presented in black and M3 in red. Cooling the sample not only reduces the value of the leakage current, but also slows its increase with fluence. This is reflected in slope values of linear fits, where $A(M2) = (2.8 \pm 0.6) \cdot 10^{-22}$ A cm^2 and $A(M3) = (7.6 \pm 0.8) \cdot 10^{-23}$ A cm^2.

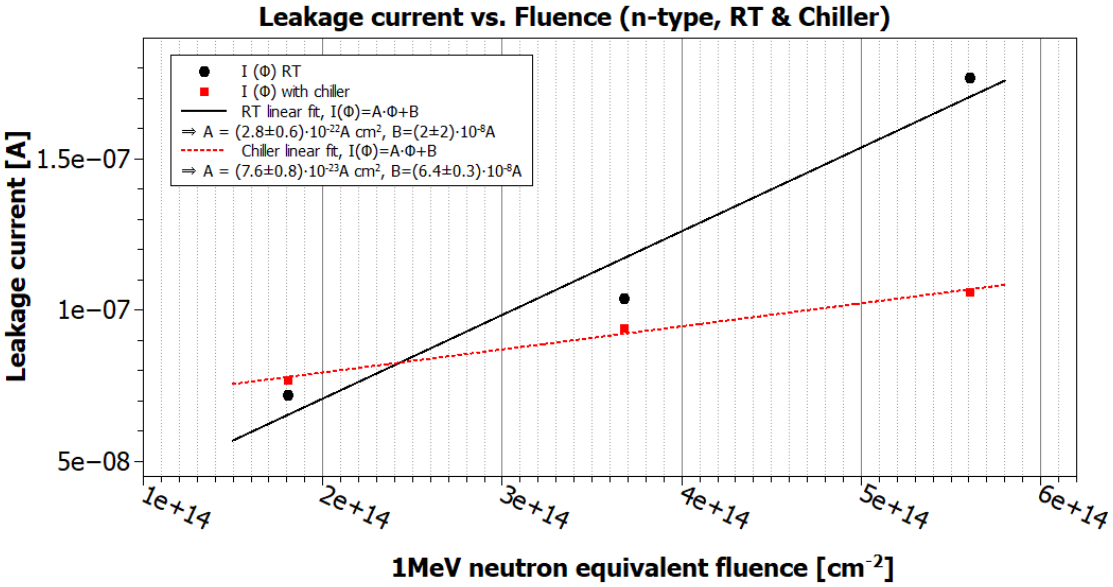

Figure 6.6: Increase in leakage current with irradiation dose (1 MeV neutron equivalent fluence) for n-type detector at RT (M2) and with chiller (M3).

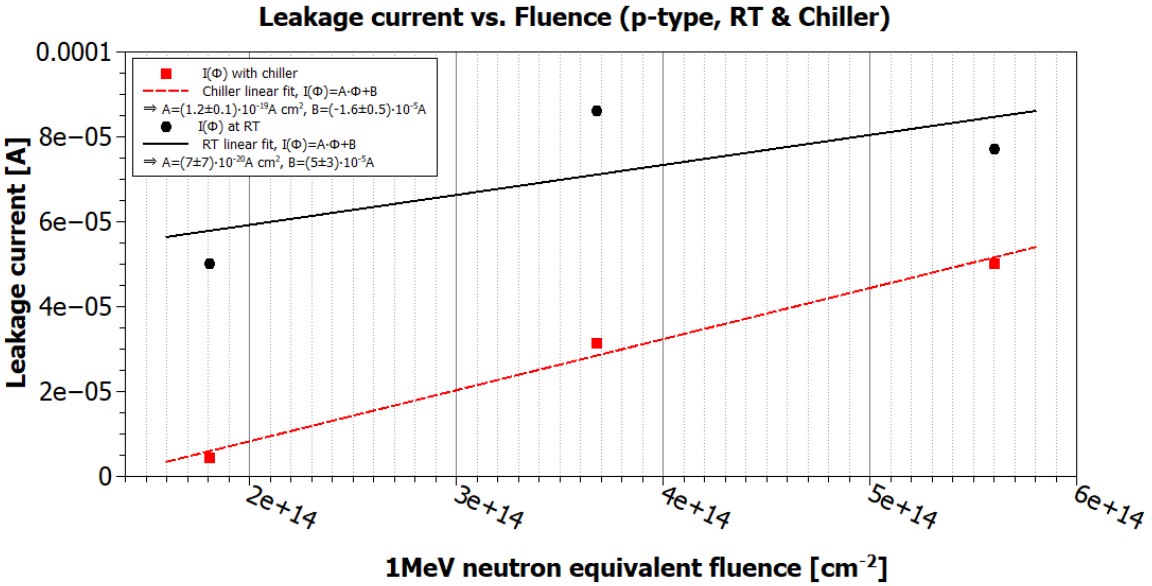

Figure 6.7: Increase in leakage current with irradiation dose (1 MeV neutron equivalent fluence) for p-type detector at RT (M2) and with chiller (M3). The leakage current from M2 measurement did not have expected linear dependance, which resulted in A(M2)=0. Samples 2 and 3, which showed deviation from expected linearity, had comparatively higher leakage current to begin with.

7 Summary and conclusions

In the course of this work, four p-type and four n-type detectors were measured with IRL and RL TCT method before and after gamma irradiation. One sample of each type was left non-irradiated, to serve as a reference for comparison of different takes of TCT measurements. The rest of the samples were sent for irradiation to RBI panoramic ^{60}Co gamma irradiation facility. Irradiation took three days in total. Each day one pair of n- and p-type detectors were taken out, and absorbed dose was recorded. Three sets of measurement conditions were analyzed: before irradiation (M1), after irradiation at room temperature (M2) and with chiller (M3).

The shapes of the current transients obtained with RL TCT measurements before and after irradiation showed no significant differences in the duration of the pulses. There was no consistent change in the amplitude, either. Both observations indicated that the CCE was not significantly degraded. In reference [35], a simulation of the CCE in n-type detectors suggests that there is 20 % charge loss at 280 V and about 15 % at 500 V for fluences around $\Phi = 2 \cdot 10^{14}$ n_{eq}/cm^2. The article from [36] agrees with this estimation and further states that the CCE starts to significantly deteriorate after fluence of $7 \cdot 10^{14}$ n_{eq}/cm ^{2}. Simulation of collected charge in n-type reverse biased detector from [36] was plotted with dotted curve in figure 7.1. As maximum fluence used (5.6·10^{14} n_{eq}/cm^2) was well under the mentioned threshold, it is within expectation that deterioration of the CCE was not yet noticeable with TCT. Behaviour of p-type samples also coincides with previous work, as article [21] reports drop of the CCE under 80 % only after ten times higher fluences than the ones used here.

Gamma irradiation of Czochralski silicon introduces positive space charge in the bulk, which increases effective space charge density N_{eff} in n-type detectors and decreases it in p-type detectors [9]. Following the relation in equation (2.8) for completely depleted bulk, full depletion voltage is proportional to N_{eff}. This means that with increasing irradiation dose, the V_{fd} increases in n-type detectors and decreases in p-type detectors made of Cz-Si. Figure 7.2 shows how N_{eff} changes with gamma irradiation dose. Since unit of Mrad is equivalent to 10 kGy, our irradiation doses fall to the very beginning of the X-axis of figure 7.2. By using the data from the plot, an

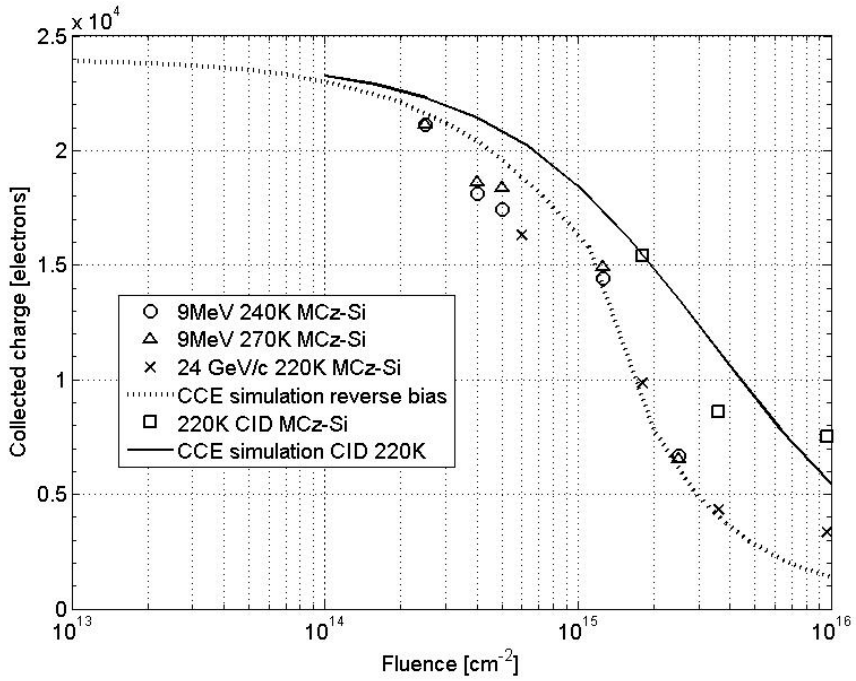

Figure 7.1: Simulation of charge collection evolution with fluence in reverse biased detectors. The simulation assumes 220 K temperature and 500 V operating voltage [36].

estimated change in n-type V_{fd} for 200 kGy gamma irradiation is

$$\frac{V_{fd}(200kGy)}{V_{fd}(0kGy)} = \frac{N_{eff}(200kGy)}{N_{eff}(0kGy)} = \frac{3.5 \cdot 10^{12}}{3.4 \cdot 10^{12}} \approx 1.03. \tag{7.1}$$

If we take the data for non-irradiated n- and p-type Sample 4 from tables 6.1 and 6.2, we can predict the expected full depletion voltage after maximum dose. For non-irradiated n-type, the V_{fd} value was multiplied by factor in equation (8.8), and for p-type the V_{fd} value was divided. But as values from different measurements differ enough to prevent direct comparison, we can also take V_{fd} values of irradiated Sample 4 and reversing the previous approach predict what would the full depletion value be if the sample had not been irradiated. Results are presented in table 7.1. The expected shift is smaller than the standard error in the measurements, meaning the change cannot be observed at this irradiation doses.

The only measurable effect of irradiation observed in this work is increase of leakage current. Linear dependance on 1 MeV neutron equivalent fluence was confirmed (see figures 6.6 and 6.7). In n-type detectors, this increase did not cause any other change in detector response. In p-type detectors leakage current was comparably higher than in n-types, as well as the noise levels. Besides preventing the TCT scan

	n-type Sample 4	p-type Sample 4
M1	225 V $\rightarrow$ 232 V	60 V $\rightarrow$ 58 V
M2	146 V $\leftarrow$ 150 V	77 V $\leftarrow$ 75 V
M3	121 V $\leftarrow$ 125 V	77 V $\leftarrow$ 75 V

Table 7.1: An evolution of the full depletion voltage due to gamma irradiation induced positive space charge in the bulk of the detectors according to simulation from [9]. The arrows point from measured to simulated value. To the left of the arrow is V_{fd} for non-irradiated detector, and to the right is for irradiated detector. Assumed gamma dose is 200 kGy.

of higher voltage range, fluctuations of total integrated charge made it impossible to determine the point of saturation. The full depletion voltage for p-type detectors had to be determined from charge integrated within full width at half maximum of the signal peak. However, the radiation induced increase of the leakage current was easily remedied by cooling the detectors.

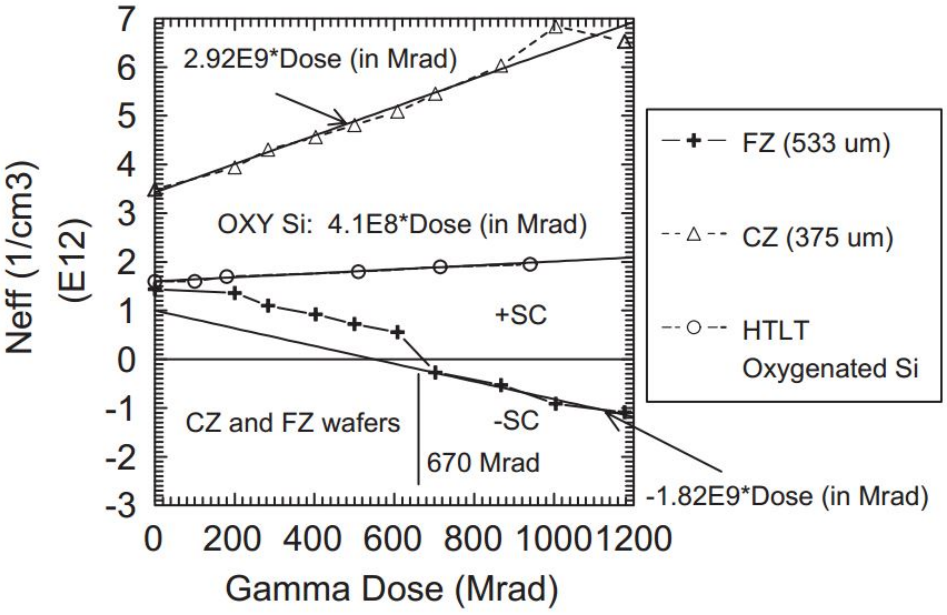

Figure 7.2: Effective space charge density as a function of gamma dose for FZ, MCz, and HTLT (high temperature, long time) oxygenated Si detectors [9]. Since 1 Mrad equals 10 kGy, gamma doses used in this work fall on the very beginning of the X-axis.

To conclude, for gamma irradiation doses up to almost 200 kGy, the studied samples showed good radiation hardness as no CCE degradation or change in V_{fd} could be observed with TCT. Considering the increase in leakage current, the n-type samples proved to be more resilient than the p-types, which makes them a better choice for gamma radiation detection.

To observe more subtle changes, more precise method should be chosen for char-

acterisation of the detectors.

Tracker system Outer Barrel Si strip detectors in CMS experiment at CERN LHC are required to withstand radiation fluences up to $1.6 \cdot 10^{14}$ n_{eq}/cm^2 after 10 years of operation. The analyzed detectors would survive this with little change. However, Inner Barrel pixels receive 10^{15} n_{eq}/cm^2 and innermost pixels 10^{16} n_{eq}/cm^2. The proposed upgrade of LHC will increase the maximal fluence to even higher values, and further endeavours to improve radiation hardness of detectors are necessary [3].

On the other hand, obtained results are already good enough for purposes of medical dosimetry [3, 41]. In radiation therapy, patients could wear Si diode dosimeters to measure the surface dose. Typical radiotherapy dose is 1 Gy in one day and that is repeated e.g. every 10-20 days. Silicon diodes studied in this work could be used at least 200 000 times before they need to be recalibrated, which is an excellent result. Simultaneously, silicon is 99 % transparent for radiotherapy photons in energy range from 5 to 20 MeV and thus does not distort X-ray radiation field a patient is subjected to. For comparison, that is more transparent than window glass is for visible light wavelengths.

Appendices

Appendix A RL TCT voltage scan of n-type samples 1-4

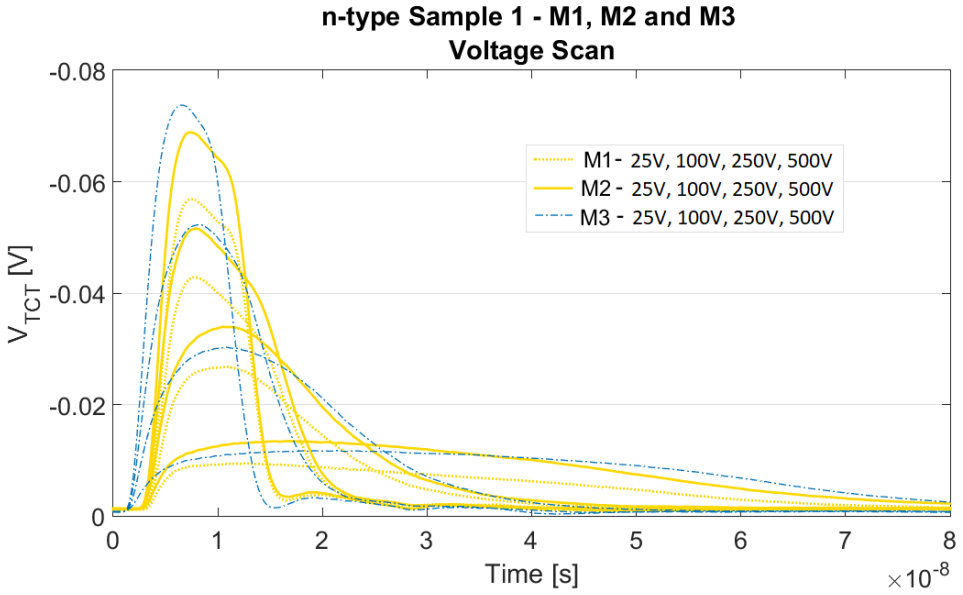

Figure A.1: TCT voltage scan with red laser at 25, 100, 250 and 500 V. Plot presents signals from n-type Sample 1 obtained in measurement sets M1 (before irradiation of Samples 2-4, room temperature), M2 (after irradiation of Samples 2-4, room temperature) and M3 (after irradiation of Samples 2-4, with chiller). Sample 1 was always measured again for reference.

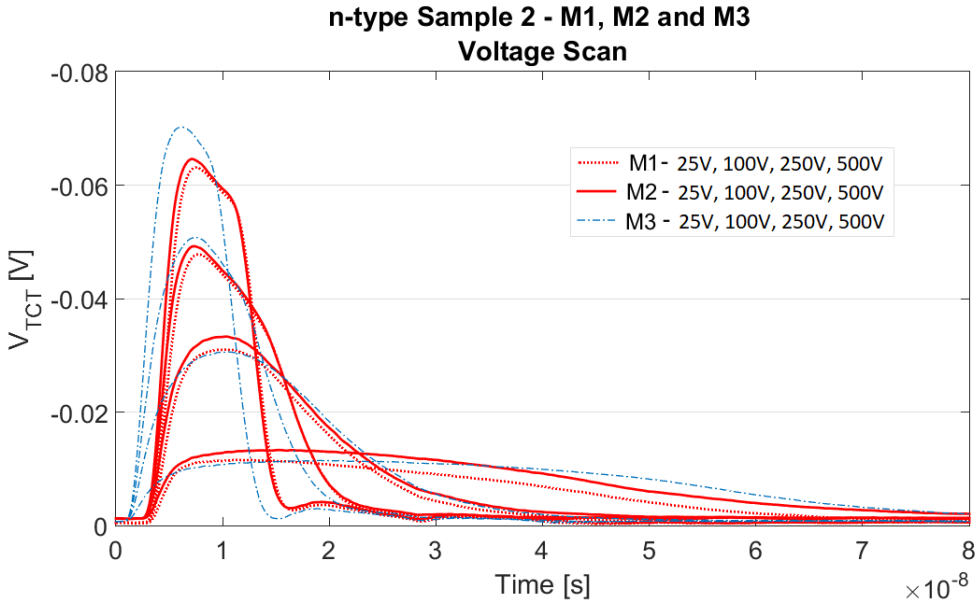

Figure A.2: TCT voltage scan with red laser at 25, 100, 250 and 500 V. Plot presents signals from n-type Sample 2 obtained in M1, M2 and M3 measurements.

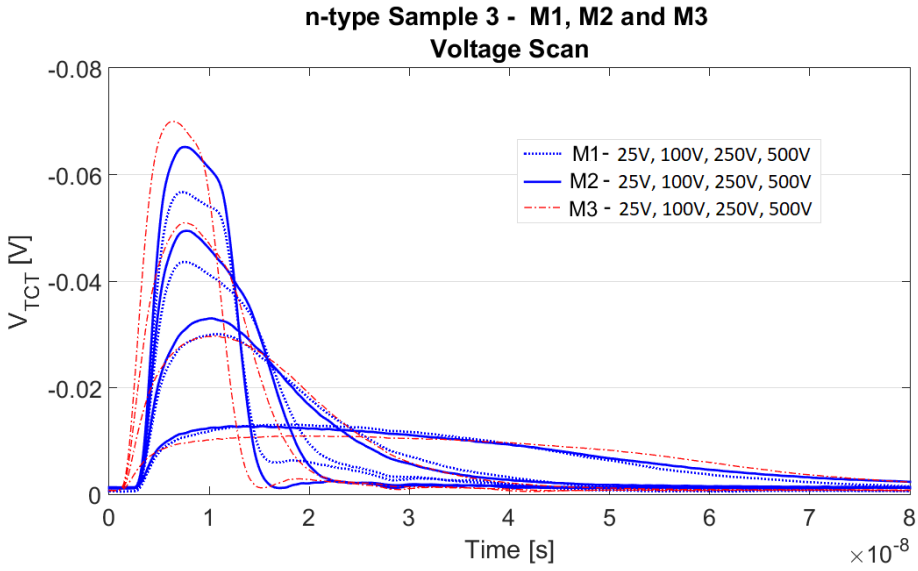

Figure A.3: TCT voltage scan with red laser at 25, 100, 250 and 500 V. Plot presents signals from n-type Sample 3 obtained in M1, M2 and M3 measurements.

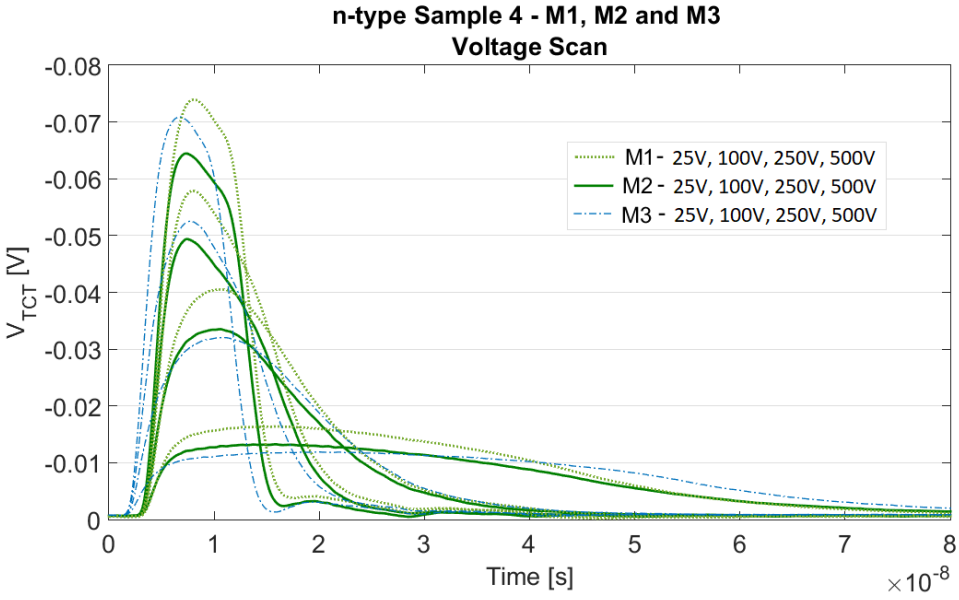

Figure A.4: TCT voltage scan with red laser at 25, 100, 250 and 500 V. Plot presents signals from n-type Sample 4 obtained in M1, M2 and M3 measurements.

Appendix B RL TCT voltage scan of p-type samples 1-4

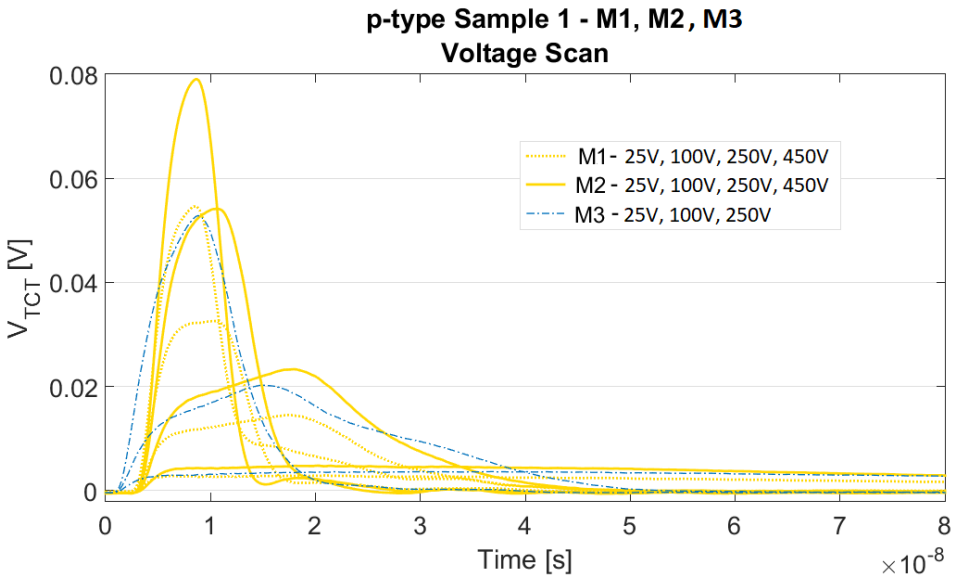

Figure B.1: TCT voltage scan with red laser at 25, 100, 250 and 450 V. Plot presents signals from p-type Sample 1 obtained in measurement sets M1 (before irradiation of Samples 2-4, room temperature), M2 (after irradiation of Samples 2-4, room temperature) and M3 (after irradiation of Samples 2-4, with chiller). Sample 1 was always measured again for reference.

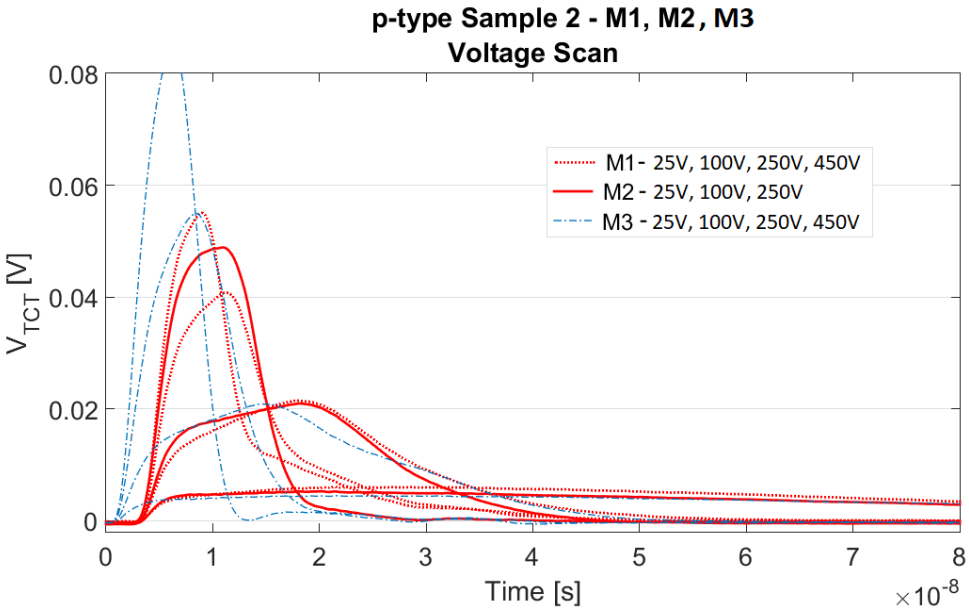

Figure B.2: TCT voltage scan with red laser at 25, 100, 250 and 450 V. Plot presents signals from p-type Sample 2 obtained in M1, M2 and M3 measurements.

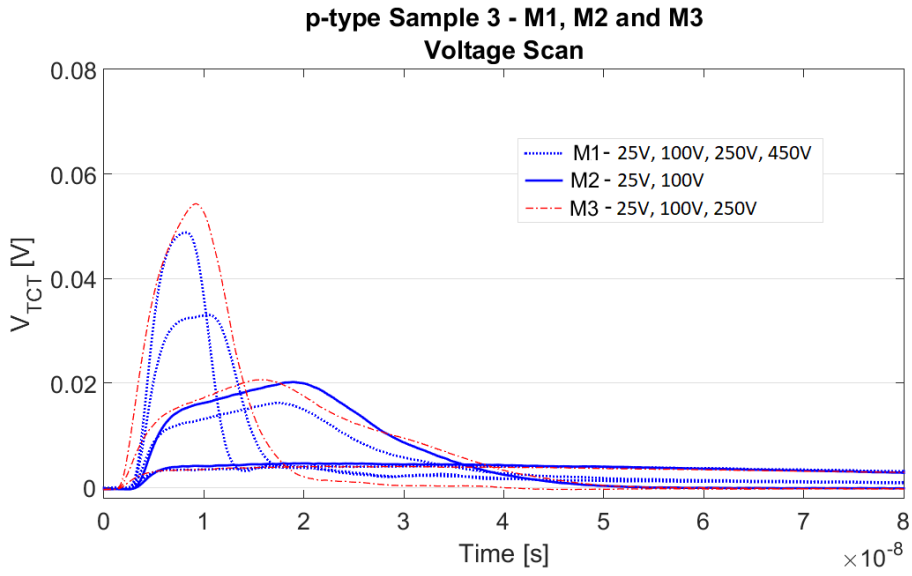

Figure B.3: TCT voltage scan with red laser at 25, 100, 250 and 450 V. Plot presents signals from p-type Sample 3 obtained in M1, M2 and M3 measurements.

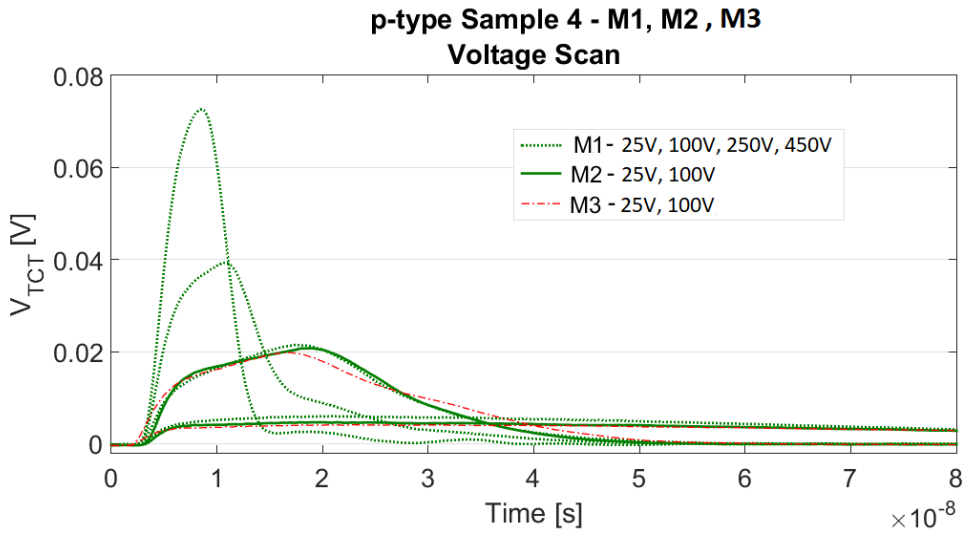

Figure B.4: TCT voltage scan with red laser at 25, 100, 250 and 450 V. Plot presents signals from p-type Sample 4 obtained in M1, M2 and M3 measurements.

Appendix C Charge-voltage plots for p-type samples

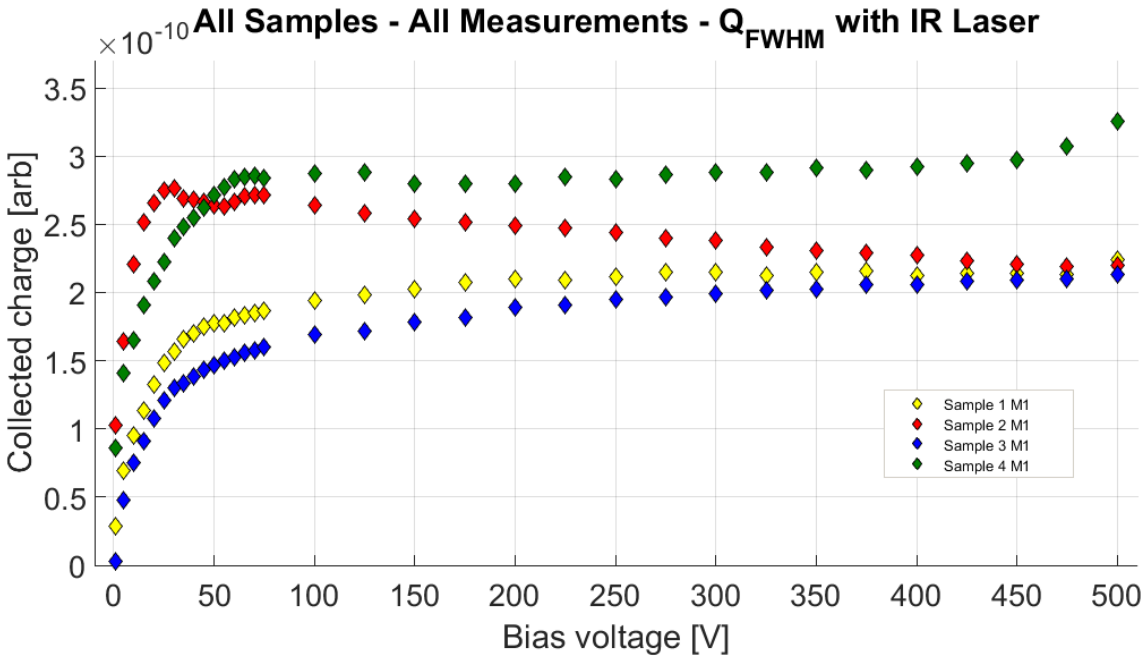

Figure C.1: Q_{FWHM}-V plot of all p-type samples from M1 measurement.

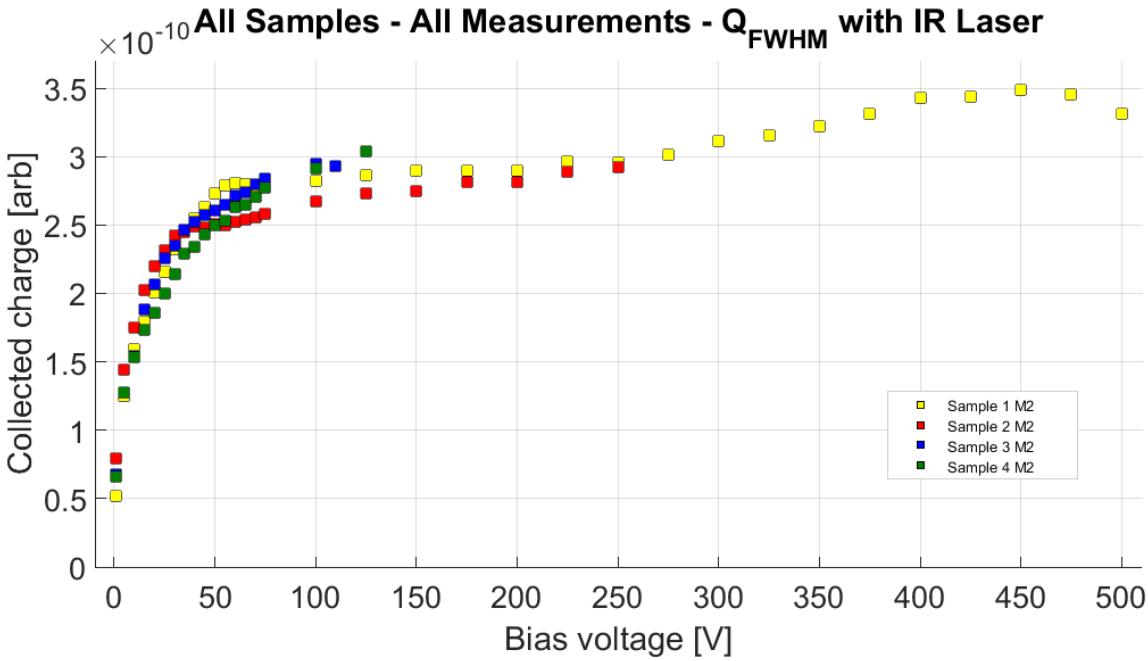

Figure C.2: Q_{FWHM}-V plot of all p-type samples from M2 measurement.

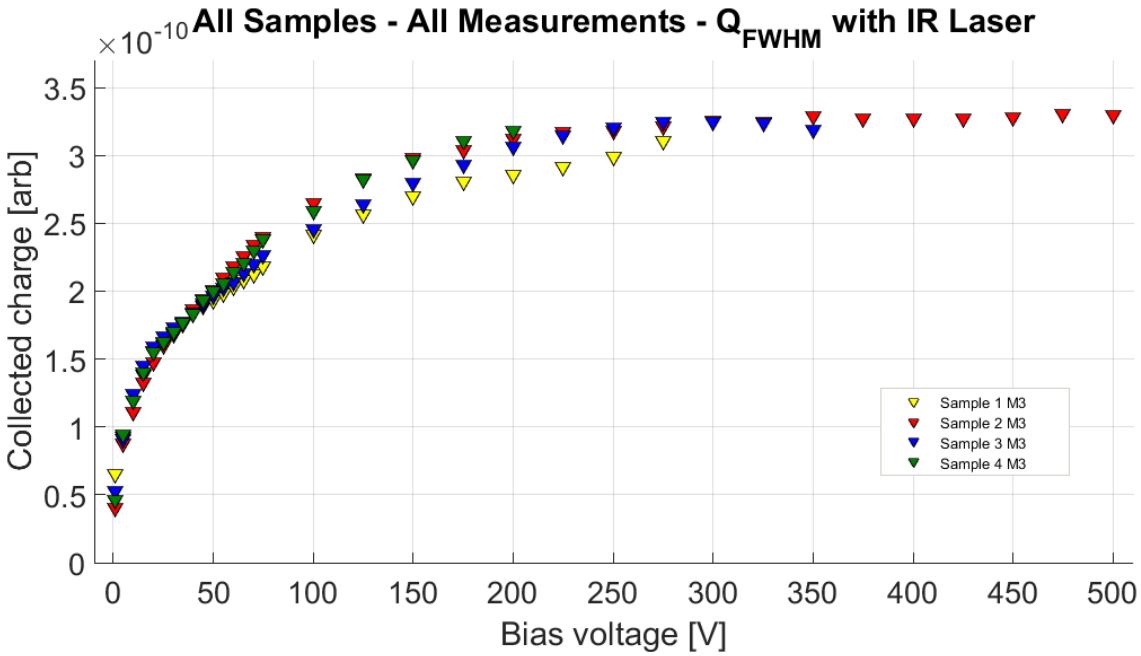

Figure C.3: Q_{FWHM}-V plot of all p-type samples from M3 measurement.

Appendix D Derivation of Shockley-Ramo theorem

Given a system of conductors, we consider two situations. First, conductors are grounded and there is a charge carrier moving in the otherwise empty space between the electrodes, as it is illustrated in figure D.1a. Potential of the electrostatic field is denoted by V_A, with $\nabla^2 V_A = 0$ in the region between the conductors. Surrounding the charge with tiny equipotential surface, Gauss' law gives:

$$-\int_S \frac{\partial V}{\partial n} da = \frac{q}{\epsilon_0}. \tag{D.1}$$

Term $\frac{\partial V}{\partial n}$ indicates differentiation with the respect to the outward normal to the sphere's surface [33]. Let the potential of the tiny sphere be V_A^q. All of the conductors are grounded, so for them $V_A^{cond.} = 0$.

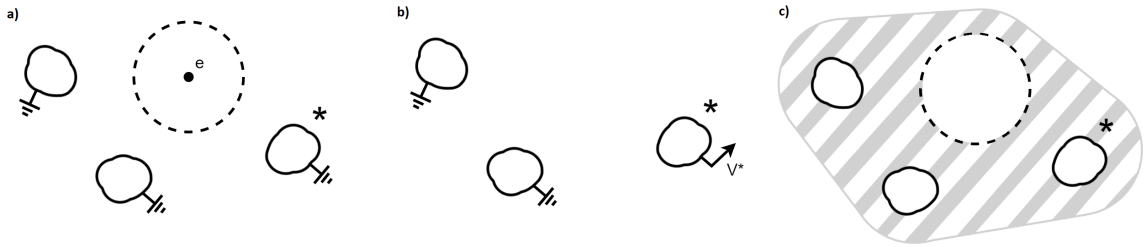

Figure D.1: a) Case A. Charge carrier is moving in otherwise empty space between grounded conductors. b) Case B. There are no charge carriers. One conductor (*) is raised to unit potential, others are grounded. c) Volume under consideration in the Green's theorem.

We consider now the other situation illustrated in figure D.1b, with charge carrier removed and all conductors save one grounded. The one conductor that is not grounded is where we want to know the induced current. It is marked with asterisk and raised to a unit potential, V_B^*. Electrostatic potential in this case is called V_B. Again, $\nabla^2 V_B = 0$, including the point where charge was positioned in the first situation. New potential on a tiny sphere at this point is V_B^q [33].

Now we use Green's theorem, mathematical theorem that stems from vector calculus:

$$\int_V \left(\Phi \nabla^2 \Psi - \Psi \nabla^2 \Phi\right) d^3x = \int_S \left(\Phi \vec{\nabla} \cdot \Psi - \Psi \vec{\nabla} \cdot \Phi\right) \cdot \hat{n} da. \tag{D.2}$$

Here, Ψ and Φ are well-behaved scalar functions, V is three-dimensional volume with volume element d^3x. S is closed two-dimensional surface bounding V, with area element da and unit outward normal $\hat{n}$ at da [42]. We apply Green's theorem to the

volume bounded by the conductors and the tiny sphere as illustrated in figure D.1c. Tiny sphere encloses charge carrier in the first case, but in the second case it is just empty space. We set $\Phi \rightarrow V_B$ and $\Psi \rightarrow V_A$. Since Laplacian of V_A and V_B iz zero in the integrating volume, left-hand side of Green's theorem is zero. Remaining surface integral may be divided into three separate contributions: tiny sphere, conductor of interest and all the other conductors. Integral over the surface of the grounded conductors is zero. Integral over conductor of interest yields the amount of charge it holds, Q^*/ϵ_0. Finally, integral over tiny sphere surface gives contribution qV_B^q/ϵ_0.

Pulling together all of these results gives us the value for charged induced on the conductor of interest by the moving unit charge:

$$Q^* = -q \cdot V_B^q. \tag{D.3}$$

From the start to the end of its path charge carrier moves through weighting potential difference ΔV_0 and thus induces in total:

$$\Delta Q = -q \cdot \Delta V_0. \tag{D.4}$$

From definitions of current and velocity, $i = dQ/dt$ and $\vec{v} = d\vec{r}/dt$, the induced current follows:

$$i = q \cdot \vec{v} \cdot \vec{E_0}(\vec{r}). \tag{D.5}$$

If charge carrier's path coincides with an equipotential of the weighting field, no current is induced [2, 33].

8 Prošireni sažetak

8.1 Uvod

Poluvodički detektori plijene pažnju od svoje pojave 60ih godina 20. stoljeća. Svega nekoliko elektronvolta potrebno je za pobuđivanje para elektron-šupljina, glavnog nosioca informacije. S obzirom da recimo ionizacijska komora treba dva reda veličine više energije za generiranje elektron-ion para, poluvodički detektori općenito nude najveću energijsku rezoluciju. Osim toga, mogu generirati brze pulseve, mali su i jednostavni za korištenje. Kako bi se predvidjelo ponašanje detektora podvrgnutih zračenju različitih vrsta i energija, nužno je pratiti kako se ozračivanjem mijenjaju njihove karakteristike. Jedna od dostupnih metoda jest metoda tranzijentne struje (*Transient Current Technique*, TCT). Pikosekundnim laserom pobude se parovi elektron-šupljina unutar osjetljivog volumena detektora i prati se signal koji nastane. U ovom radu korišteni su crveni i infracrveni laseri valnih duljina 660 i 1064 nm. Iz nastalih signala moguće je odrediti napon potpunog osiromašenja, prikupljeni naboj, raspodjelu električnog polja unutar volumena detektora, predznak prostornog naboja, učinkovitost prikupljanja naboja i efektivno vrijeme zatočenja.

8.2 Pn-spoj i zona osiromašenja

Poluvodiči n-tipa imaju višak elektrona koji dolazi od dopiranja donorskim elementima poput fosfora, arsena ili antimona. S druge strane, dopiranje akceptorskim elementima poput galija, bora ili indija uvodi veliku koncentraciju šupljina u materijal i za takav poluvodič kažemo da je p-tipa. Kada bi se u poluvodič dopiran jednom vrstom nečistoća difuzijom uvela druga vrsta, došlo bi do stvaranja tzv. pn-spoja. U gruboj aproksimaciji možemo pretpostaviti nagli prijelaz s recimo n- na p-tip poluvodiča. Na strani n-tipa postoji visoka koncentracija elektrona, a na strani p-tipa visoka koncentracija šupljina. Dolazi do difuzije nosioca naboja na suprotnu stranu pn-spoja, gdje se rekombiniraju. Na taj način stvara se područje osiromašenja u kojem nema slobodnih nosioca naboja. Preostala fiksna raspodjela prostornog naboja stvara električno polje koje zaustavlja daljnju difuziju elektrona i šupljina. Ako se p-strana pn-spoja spoji na negativni napon, a n-strana uzemlji, prirodno prisutno električno polje dodatno se naglašava i zona osiromašenja se proširuje. Ako su koncentracije

donora i akceptora na granici pn-spoja drastično različite, zona osiromašenja se dominantno proteže na slabije dopiranu stranu. Pod tom pretpostavkom, rješavanjem Poissonove jednadžbe uz odgovarajuće rubne uvjete možemo dobiti izraz za širinu zone osiromašenja [1, 2]:

$$d \cong \sqrt{\frac{2\epsilon V}{eN_{eff}}}. \tag{8.6}$$

Dielektrična konstanta materijala označena je sa ϵ, e je jedinični naboj, V apsolutna vrijednost napona na pn-spoju, a N_{eff} efektivna koncentracija dopiranih nečistoća u zoni osiromašenja.

Izostanak slobodnih nosioca naboja omogućava zračenjem generiranim parovima elektron-šupljina da se uz puno manje sudara kreću kroz zonu osiromašenja. Električno polje ih ubrzava prema elektrodama, na kojima svojim gibanjem induciraju signal. Opisani proces prikazan je na slici 8.2.

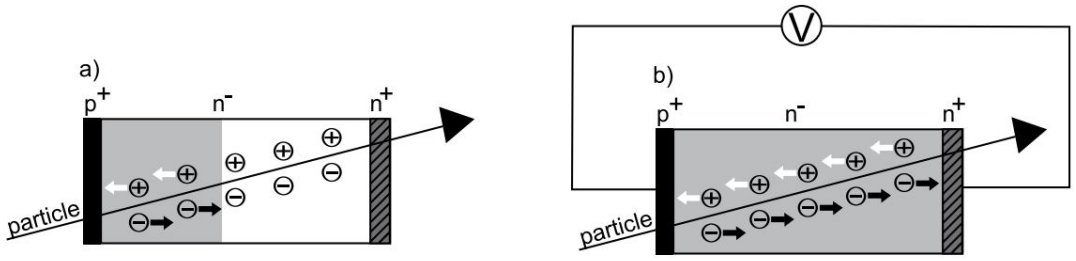

Slika 8.2: a) Elektroni i šupljine generirani u području osiromašenja brzo su prikupljeni na elektrodama. U ostatku n^- volumena nema električnog polja, generirani naboji nasumično se gibaju kroz kristal i ne doprinose indukciji signala; b) Reverzna polarizacija detektora omogućava širenje osjetljive zone na cijeli dostupni volumen [5].

Zona osiromašenja je osjetljivi volumen poluvodičkih detektora. Ograničena je ukupnom debljinom detektora. Ako se proteže kroz cijeli dostupni volumen, kažemo da je detektor potpuno osiromašen. Napon potreban da bi se to ostvarilo zove se napon potpunog osiromašenja V_{fd} (*full depletion*).

8.3 Interakcija zračenja s materijom i otpornost detektora na zračenje

Gubitak energije nabijenih čestica tijekom prolaska kroz materiju pretežno je posljedica neelastičnih ionizacijskih sudara s atomskim elektronima. Tzv. zaustavna moć materijala dE/dx opisana je semiempirijskom Bethe-Blochovom jednadžbom, a karakteristični primjer krivulja za nekoliko različitih materijala prikazan je na slici 8.3. Pos-

toji energija na kojoj je zaustavna moć minimalna moguća. Takve se čestice nazivaju minimalno ionizirajuće (*minimum ionizing particle*, MIP).

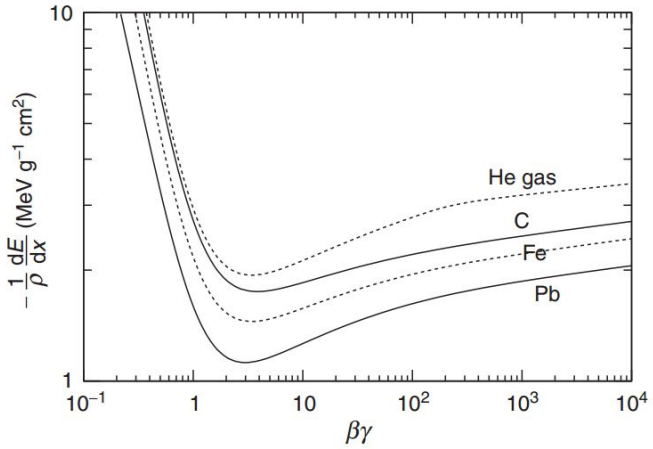

Slika 8.3: Zaustavna moć olova, željeza, ugljika i plinovitog helija za jednostruko nabijene čestice [12]. Krivulja za silicij nalazi se između krivulja željeza i ugljika.

Fotoni kao neutralne čestice interagiraju preko drugih mehanizama: fotoelektričnog efekta, Comptonskog raspršenja i produkcije parova. Fotoelektrični efekt i produkcija parova potpuno uklanjaju foton, a energiju preuzimaju nabijene čestice (elektron kod fotoefekta, odnosno elektron-pozitron par kod produkcije parova). Dio energije odboja preuzima i jezgra, radi očuvanja impulsa. U Comptonskom raspršenju foton se rasprši na elektronu predajući mu samo dio energije. Ostatak energije odnosi novi foton. Vjerojatnost apsorpcije fotona u siliciju prikazana je na slici 8.4. Na energijama od nekoliko MeV-a dominira upravo Comptonsko raspršenje.

Samostalni atom ima kvantizirane atomske energijske nivoe. Ako bi u njegovu blizinu doveli drugi identični atom, došlo bi do cijepanja nivoa u dva molekulska s energijama malo različitim od početnih atomskih enregija, zbog Paulijevog principa isključenja koji diktira da se elektroni ne mogu nalaziti u istom kvantnom stanju. U kristalu se u uređenoj rešetci na međusobnoj udaljenosti od nekoliko angstrema nalazi neki broj N atoma (reda veličine 10^{23} cm^{-3}). Analogno sitaciji s dva atoma, dolazi do cijepanja atomskih nivoa u N novih energijskih nivoa. Novih stanja ima taman dovoljno da se sva mogu popuniti elektronima. S obzirom na vrlo velik broj nivoa, energijski su oni vrlo blizu i možemo reći da su nastale kontinuirane energijske vrpce. No postoje i energije na kojima nema dostupnih energijskih stanja, što nazivamo zabranjenim pojasom. U pojednostavljenoj slici možemo govoriti o valent-

nom i vodljivom pojasu i zabranjenoj zoni između njih. Kad ne bi bilo termalnih pobuđenja, valentna vrpca u poluvodičima bila bi potpuno popunjena, a vodljiva prazna. No ako se elektronima preda dovoljno energije, oni mogu prijeći u vodljivi pojas i slobodno se kretati u kristalu neograničeni vezom za pojedini čvor kristalne rešetke. Gdje se elektron nalazio u valentnoj vrpci ostalo je prazno energijsko stanje, što možemo tretirati kao novu česticu - šupljinu. Prema tome, pobuđivanjem elektrona iz valentnog u vodljivi pojas nastao je par slobodnih čestica, elektron i šupljina. Ionizacijske interakcije upadnog zračenja generiraju parove elektron-šupljina. Da bi se čestica opazila silicijskim detektorom, nužno je posredstvo nabijenih čestica. No osim reverzibilnih ionizacijskih interakcija, zračenje može imati i trajnije posljedice na kristalnu strukturu. Neionizacijski prijenosi energije stvaraju Frenkelove parove. Atom kristalne rešetke primi dovoljno energije da bude izbačen sa svog položaja, a na njegovom mjestu ostane praznina. U slučaju da izbačeni atom ima dovoljno energije, duž svoje putanje može stvarati nove Frenkelove parove. Atomu silicija treba predati minimalno 25 eV da bi ga se izbacilo iz pravilne kristalne rešetke. Defekti su pokretni i mogu se kombinirati u kompleksnije strukture. Svako odstupanje od idealne kristalne rešetke odražava se na strukturi energijskih nivoa. Unutar zabranjenog pojasa energija javljaju se energijska stanja. Ovisno o njihovom položaju u odnosu na energijske vrpce, moguće posljedice su: povećanje struje kroz detektor u nepropusnoj polarizaciji, promjene efektivnog dopiranja osjetljivog volumena detektora (a time i promjene napona potrebnog za potpuno osiromašenje), gubitak naboja zbog zatočenja na defektima. Eksperimentalno je uočeno da je porast struje proporcionalan s apsorbiranom dozom zračenja (izraženom u jedinici n_{eq}/cm^2).

U nastojanju da se poboljša otpornost detektora na utjecaj zračenja, razvijeno je nekoliko različitih pristupa. Razmatra se upotreba različitih materijala i konfiguracija, obogaćivanje materijala korisnim nečistoćama te variranje radnih uvjeta. U ovom radu korištene su po četiri silicijske diode n-tipa ($p^+/n^-/n^+$) i p-tipa ($n^+/p^-/p^+$) napravljene od Czochralskog silicija koji ima veliki udio kisika, oko $10^{17} - 10^{18}$ cm^{-3}. Istraživanja su pokazala da kisik ima povoljno djelovanje na otpornost na gama zračenje.

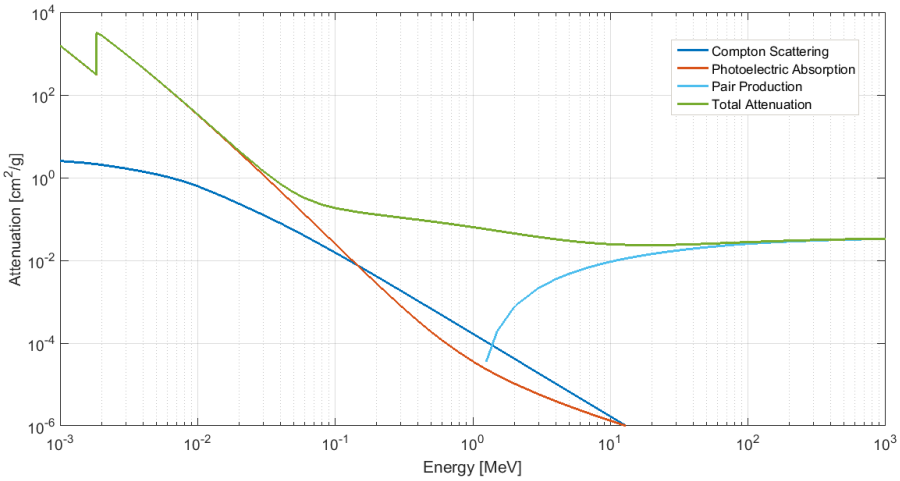

Slika 8.4: Vjerojatnost apsorpcije X-zračenja u siliciju za tri glavne interakcije fotona. Za izradu grafa korišteni su podaci iz baze podataka NIST XCOM: Photon Cross Sections Database [11].

8.4 Metode i materijali

Silicijski detektori korišteni u izradi ovog diplomskog rada su jednostavne diode nesegmentiranih elektroda napravljene u finskom centru za nanotehnologiju Micronova. Namijenjeni su za testiranje, pa se na prednjoj strani nalazi optički otvor koji omogućava prodiranje laserskog snopa do aktivnog volumena detektora. Glavna struktura može se podijeliti na aktivni dio i zaštitni prsten koji definira aktivni dio i smanjuje utjecaj površinskih struja. U standardnoj konfiguraciji, napon se dovodi na stražnju elektrodu, dok se s uzemljene prednje elektrode opaža signal. Fotografija jednog od korištenih uzoraka s označenim dijelovima nalazi se na slici 8.5a.

Za istraživanje karakteristika detektora korištena je metoda tranzijentne struje. Infracrveni laser prodire kroz cijelu debljinu detektora (300 μm) i simulira prolazak minimalno ionizirajuće čestice. Na nastali signal podjednako utječu elektroni i šupljine. Crveni laser, s druge strane, prodire svega nekoliko mikrometara u uzorak. Pod pretpostavkom da se optički otvor nalazi s prednje strane, kao u korištenim uzorcima, struja u detektoru n-tipa potjecat će dominantno od gibanja elektrona, a u p-tipu od gibanja šupljina.

Formiranje pulsa počinje čim se zračenjem generirani naboji počnu kretati prema elektrodama. Proces završava kada se na elektrodi prikupi i zadnji naboj. Iz Shockley-Ramo teorema, koji opisuje način računanja trenutne inducirane struje na elektrodi zbog gibanja jednog naboja, možemo dobiti izraz za vremenski ovisan razvoj pulsa

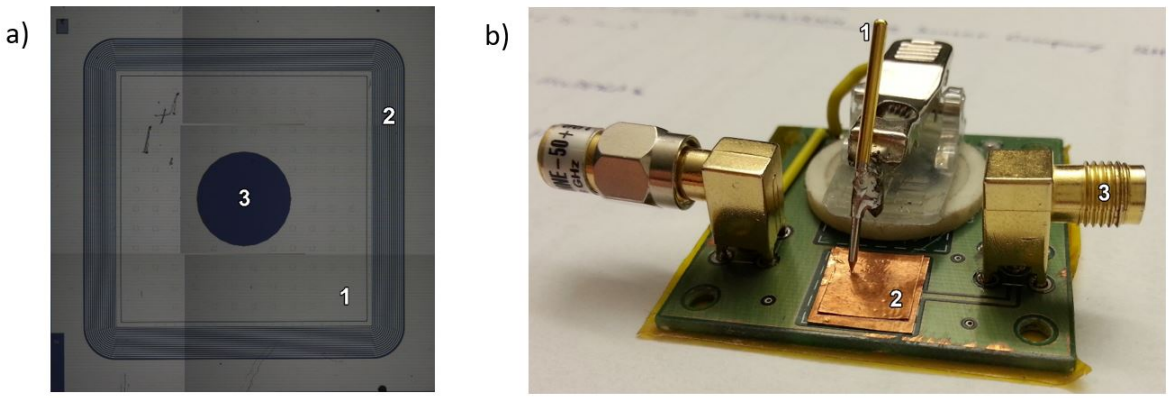

Slika 8.5: a) Slika jednog od detektora n-tipa sastavljena od šest pojedinačnih uvećanih fotografija. U sredini nesegmentirane elektrode (1) nalazi se optički otvor (3), a detektor obrubljuje sustav zaštitinih prstenova (2); b) Držač uzorka. Detektor se pomoću igle (1) pričvrsti na bakrenu pločicu (2). Pločica dovodi napajanje na stražnju stranu detektora. S istog Lemo kabela koji dovodi napon na bakrenu pločicu očitava se inducirani signal. Konektor za Lemo kabel označen je sa (3).

zbog $N_{e,h}$ nosioca naboja generiranih u trenutku t_0:

$$I_{e,h}(t) = \frac{e}{w} \cdot N_{e,h}(t_0) e^{-\frac{t-t_0}{\tau_{eff}{}^{e,h}}} \cdot \mu_{e,h} E(x). \tag{8.7}$$

U navedenoj formuli, w je ukupna debljina detektora, μ je mobilnost, $E(x)$ je raspodjela električnog polja unutar zone osiromašenja u detektoru. Eksponencijalni faktor uzima u obzir utjecaj zatočenja na gubitak naboja, a τ_{eff} je efektivno vrijeme koje čestica provede slobodna prije nego se zatoči na nekom defektu. Vrijeme za formiranje signala je ograničeno, pa zatočenje općenito uzrokuje gubitak naboja i smanjuje efikasnost njegovog prikupljanja (*charge collection efficiency*, CCE). Električno polje je maksimalno na samom prijelazu s n- na p-stranu detektora, pa će nosioci naboja ubrzani na tom mjestu dati veliki doprinos signalu. Ako kao posljedica ozračivanja osjetljivi volumen detektora promijeni efektivno dopiranje (npr. dogodi se prijelaz s n- na p-tip), maksimum polja prelazi na suprotnu stranu i to će se odraziti na oblik signala. Širina pulsa mjera je vremena prikupljanja nosioca naboja. Ako puls nakon ozračivanja traje znatno kraće, to je jedan od ukazatelja smanjenja CCE. Ove informacije pruža TCT analiza crvenim laserom.

Integracija signala dobivenog analizom uzoraka infracrvenim laserom daje mjeru prikupljenog naboja pri prolasku minimalno ionizirajuće čestice. Ako nema gubitaka, prikupljeni naboj proporcionalan je debljini zone osiromašenja. Prema jednadžbi (8.6), zona osiromašenja raste kao korjen nametnutog napona. Kada se proširi kroz

cijelu dostupnu debljinu detektora, prikupljeni naboj saturira s daljnim povećanjem napona. To je demonstrirano na slici 8.6. Prikazan je integrirani naboj jednog od uzoraka n-tipa s prilagodbom na korjensku funkciju prije i linearnu nakon saturacije. Naboj je integriran na dva načina. Q_{tot} integrira cijeli zabilježeni puls, dok Q_{FWHM} integrira samo naboj ispod pune širine na pola maksimuma pulsa (*full width at half maximum*, FWHM). Kako Q_{FWHM} ne uzima u obzir sav prikupljeni naboj, saturacija je sporija, ali na dobivene krivulje manje utječe šum mjerenja. To se pokazalo od iznimne važnosti za analizu detektora p-tipa, kojima je nakon ozračivanja šum onemogućio određivanje točke saturacije (a time i napona potpunog osiromašenja V_{fd}) iz Q_{tot} podataka. Detektori n-tipa nisu imali taj problem i njima se V_{fd} određivao iz ukupno integriranog naboja.

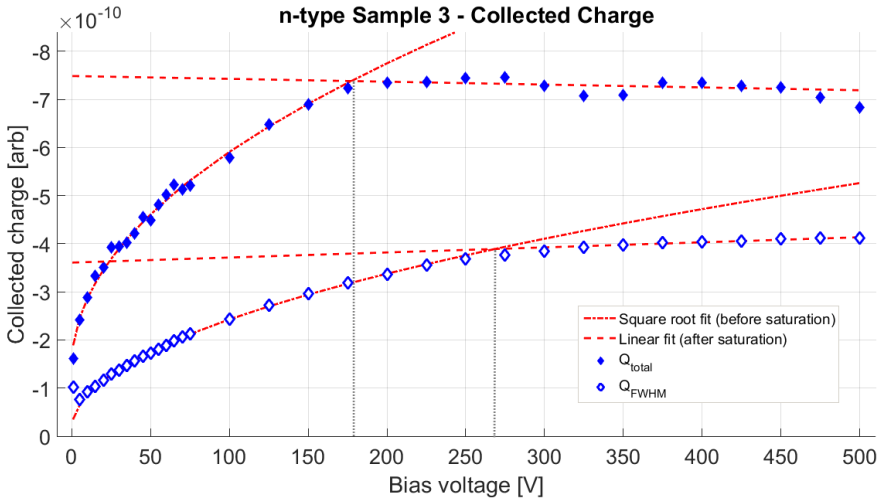

Slika 8.6: Graf prikazuje ovisnost prikupljenog naboja o naponu na detektoru. Q_{tot} predstavlja naboj sadržan u cijelom pulsu, a Q_{FWHM} je naboj sadržan unutar FWHM pulsa. Prije saturacije naboj se mijenja kao korjen nametnutog napona. Pošto FWHM integracija signala zanemaruje dio prikupljenog naboja, saturacija je sporija.

Postupak za određivanje napona potpunog osiromašenja uključuje prilagodbu linearne funkcije na krivulju prije i nakon saturacije. Kako bi se jasnije naglasila tražena promjena funkcionalne ovisnosti o naponu, korištena je logaritamska skala na x-osi (napon). Izmjerena točka najbliža sjecištu pravaca uzima se kao V_{fd}.

TCT skeniranje provedeno je u rasponu od 1 do 500 V, ako je to bilo moguće. Polaritet napona je pozitivan za n-tip detektora, a negativan za p-tip. U rasponu od 1 do 75 V korak je bio 5 V, a za vrijednosti više od toga 25 V.

Uzorci su ozračeni na Institutu Ruđer Bošković u postrojenju za panoramsko gama-ozračivanje ^{60}Co. Dominantne energije gama zraka iz raspada ^{60}Co su 1.1732

MeV i 1.3325 MeV. Na ovim energijama u siliciju dominira gubitak energije preko Comptonskog raspršenja. Emitirani Comptonski elektroni mogu uzrokovati oštećenja kristalne strukture. Apsorbirana doza mjeri ukupnu energiju apsorbiranu po jedinici mase. Mjerna jedinica je 1 Gray (Gy) = 1 J/kg. Uzorci su prema rastućoj primljenoj dozi označeni brojevima od 1 do 4, uz napomenu da uzorci 1 n- i p-tipa nisu ozračeni i korišteni su kao referentno mjerenje. Ozračivanje preostalih uzoraka trajalo je tri dana. Svaki dan bi se po jedan n- i p- uzorak izvadio i zabilježila bi se apsorbirana doza nakon toga dana. Pojedinačne i ukupne apsorbirane doze prikazane su u tablici 8.1.

	Dan 1	Dan 2	Dan 3	Ukupna doza	1 MeV n_{eq} doza
Uzorak 1 (n33, p8)	-	-	-	0	0
Uzorak 2 (n12, p3)	60.102	-	-	60.102	$1.80 \cdot 10^{14}$
Uzorak 3 (n26, p7)	60.102	62.461	-	122.563	$3.68 \cdot 10^{14}$
Uzorak 4 (n21, p6)	60.102	62.461	64.187	186.750	$5.60 \cdot 10^{14}$

Tablica 8.1: Apsorbirana doza u kGy za n- i p-tipove detektora nakon ozračivanja ^{60}Co. Posljednji stupac prikazuje ukupnu dozu u jedinici 1 MeV neutronskog ekvivalenta po cm^2.

8.5 Rezultati

Kraticama M1, M2 i M3 označena su tri seta TCT mjerenja provedena s crvenim i infracrvenim laserom. M1 mjerenje obavljeno je na sobnoj temperaturi prije, a M2 nakon ozračivanja uzoraka 2-4. M3 mjerenje obavljeno je nakon ozračivanja uzoraka 2-4, ali uz hlađenje na temperaturu u prosjeku 10 °C nižu od sobne.

Analiza oblika signala iz TCT mjerenja crvenim laserom

Za detektore n-tipa, signali dobiveni TCT analizom crvenim laserom nisu pokazivali konzistentne promjene amplitude i trajanja signala s povećanjem doze gama ozračivanja. Za sve setove mjerenja na 250 V, vrijeme prikupljanja elektrona u uzorcima kretalo se između 17 i 19 ns. Amplituda signala na višim vrijednostima napona razlikovala se između pojedinih setova mjerenja, ali usporedbom s rezultatima neozračenog uzorka ustanovilo se da su promjene posljedica varijacija u samim TCT mjerenjima. Signali uzorka 3 n-tipa izmjereni na 25, 100, 250 i 500 V prikazani

su na slici 8.7 za sva tri seta mjerenja. Silazni oblik svih signala ukazuje da se maksimum električnog polja nalazi uz prednju elektrodu i da je osjetljivi volumen detektora n-tipa i nakon najviše apsorbirane doze zračenja.

Od detektora p-tipa, samo je uzorak 2 dosegao dovoljno visoke napone gdje se počinju uočavati varijacije u amplitudi. Signali nakon ozračivanja uzorka 2 bili su konzistentno manje amplitude u odnosu na neozračeno mjerenje. Vrijeme prikupljanja šupljina u detektorima p-tipa kretalo se između 14 i 19 ns, ponovno bez značajne promjene s apsorbiranom dozom zračenja.

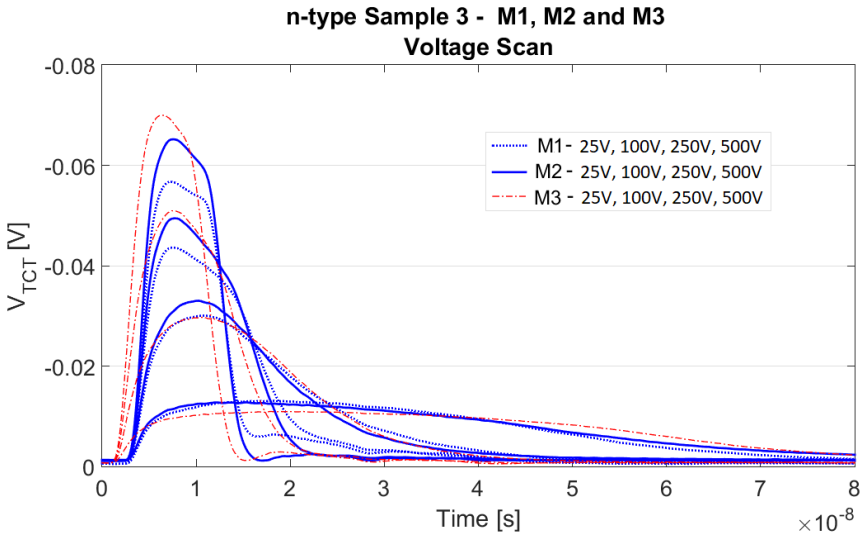

Slika 8.7: Signali dobiveni TCT analizom crvenim laserom uzorka 3 n-tipa. Prikazani su signali izmjereni na 25, 100, 250 i 500 V u sva tri seta mjerenja.

Određivanje V_{fd} iz TCT mjerenja infracrvenim laserom

Rezultati određivanja napona potpunog osiromašenja metodom opisanom u prethodnom poglavlju nalaze se u tablici 8.2 za uzorke n-tipa i u tablici 8.3 za uzorke p-tipa.

Nepouzdanost korištene metode za procjenu V_{fd} bila je jedna mjerna točka kod n-tipa detektora, i 3 točke kod p-tipa na vrijednostima nižim od 75 V. Standardna devijacija je prema tome 25 V za uzorke n-tipa i 15 V za gotovo sve uzorke p-tipa. Ako vrijednosti neozračenih uzoraka držimo kao indikaciju razlike u samim setovima mjerenja, preostale vrijednosti ne pokazuju statistički značajne promjene V_{fd} vrijednosti kao posljedicu gama ozračivanja detektora. To je vidljivo i na Q-V grafu prikazanom na slici 8.8 za uzorak 3 n-tipa. Osim samih razlika između M1, M2 i M3 mjerenja, krivulje prikupljenog naboja vrlo su slične za sve uzorke unutar istog

mjernog seta. U neozračenim uzorcima je to očekivano, pošto su svi korišteni detektori n-tipa napravljeni tijekom istog procesa proizvodnje. Isto vrijedi i za korištene detektore p-tipa. Vrlo slični odgovor detektora čak i nakon doze od gotovo 200 kGy, dodatna je potvrda njihove izdržljivosti u ovim rasponima gama ozračivanja.

n-tip	Uzorak 1	Uzorak 2	Uzorak 3	Uzorak 4
M1	175 V	175 V	175 V	225 V
M2	125 V	100 V	125 V	150 V
M3	125 V	125 V	125 V	125 V

Tablica 8.2: Napon potpunog osiromašenja za uzorke n-tipa. Standardna pogreška je 25 V za sve vrijednosti u tablici.

p-tip	Uzorak 1	Uzorak 2	Uzorak 3	Uzorak 4
M1	50 V	25 V	30 V	60 V
M2	60 V	35 V	50 V	75 V
M3	75 V	100 V	75 V	75 V

Tablica 8.3: Napon potpunog osiromašenja za uzorke p-tipa. Standardna pogreška je 25 V za mjerenje M3 uzorka 2, a 15 V za sve ostale vrijednosti.

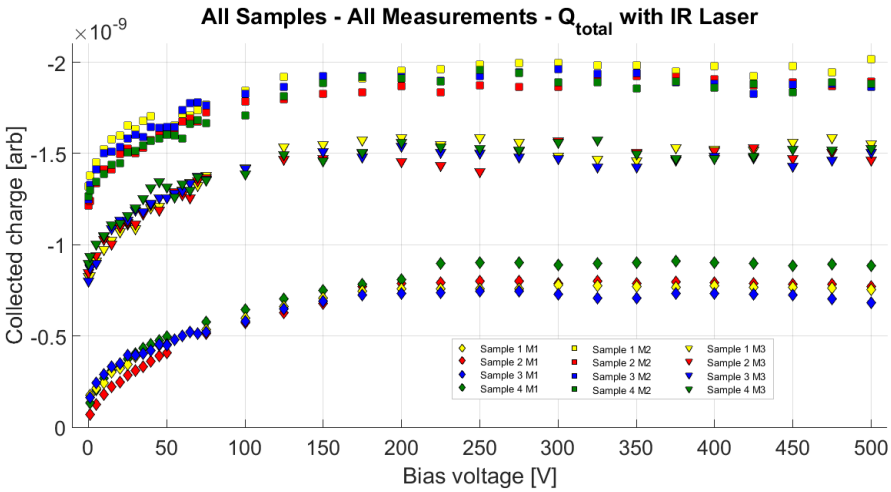

Slika 8.8: Graf prikazuje ovisnost ukupnog prikupljenog naboja o naponu na detektoru, za sve uzorke n-tipa u svim setovima mjerenja. Integrirani su signali dobiveni TCT analizom s infracrvenim laserom, čime se simulira prolazak minimalno ionizirajuće čestice kroz detektor.

Utjecaj ozračivanja na struju kroz detektor u reverznoj polarizaciji

Eksperimentalno je opaženo da s porastom apsorbirane doze zračenja struja kroz detektor u reverznoj polarizaciji pokazuje linearni porast. Ovaj poznati empirijski

rezultat vrijedi samo za potpuno osiromašene detektore. Za prilagodbu na linearnu funkciju oblika $I_{leak}(\Phi) = A \cdot \Phi + B$ korištene su vrijednosti struje kroz uzorke 2-4 očitane na naponima iznad V_{fd}. Za uzorke p-tipa odabrane su vrijednosti na 100 V, a za uzorke n-tipa na 200 V. Metoda najmanjih kvadrata korištena je za prilagodbu linearne funkcije na podatke posebno iz M2 mjerenja, i posebno iz M3. Hlađenje uzorka tijekom M3 mjerenja smanjilo je iznos struje kroz detektor, što se odrazilo na smanjenoj vrijednosti nagiba pravca u odnosu na rezultate analize M2 mjerenja.

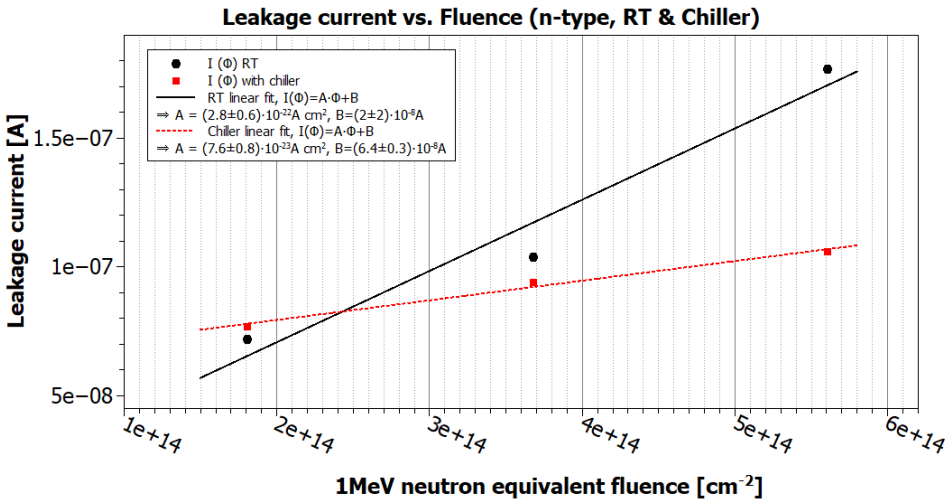

Slika 8.9: Porast struje kroz detektor u reverznoj polarizaciji u ovisnosti o apsorbiranoj dozi zračenja izraženoj u mjernoj jedinici 1 MeV n_{eq}/cm^2. Prikazani su podaci iz M2 i M3 mjerenja detektora n-tipa.

Detektori p-tipa pokazivali su brzi porast u struje reverzne polarizacije. Uzorci 2 i 3 i prije ozračivanja su imali višu struju (0.504 μA i 0.082 μA) u usporedbi s uzorcima 1 i 4 (0.031 μA i 0.034 μA). To se odražavalo i u M2 mjerenju, pa je prilagodba linearne funkcije na podatke dala rezultat $A(M2) \approx 0$. Hlađenje je smanjilo struju dovoljno da linearna ovisnost postane uočljiva. Za M3 mjerenje uzoraka p-tipa, nagib pravca iznosi $A(M3) = (1.2 \pm 0.1) \cdot 10^{-19}$ A cm^2.

Linearna ovisnost struje kroz detektor o apsorbiranoj dozi zračenja (u mjernoj jedinici 1 Mev n_{eq}/cm^2) jasno je vidljiva i u uzorcima n-tipa. Za M2 mjerenja, dobiveni nagib pravca iznosi $A(M2) = (2.8 \pm 0.6) \cdot 10^{-22}$ A cm^2, a iz M3 mjerenja dobilo se $A(M3) = (7.6 \pm 0.8) \cdot 10^{-23}$ A cm^2.

Slika 8.9 prikazuje očitane vrijednosti struje kroz detektore n-tipa s pripadnim linearnim funkcijama prilagodbe. M2 mjerenja prikazana su crnom bojom, a M3 crvenom.

Porast struje u reverznoj polarizaciji jedini je opaženi utjecaj absorbiranih doza gama zračenja na korištene detektore.

8.6 Zaključak

Iz oblika TCT pulsa dobivenih crvenim laserom zaključeno je da uzorci ne pokazuju znakove degradacije čak ni nakon gotovo 200 kGy, što je maksimalna doza zračenja kojoj su bili izloženi.

Simulacija efikasnosti prikupljanja naboja iz prijašnjih istraživanja [35] predviđa smanjenje CCE u detektorima n-tipa za 20 % na naponu 280 V i za 15 % na 500 V, nakon apsorbirane doze $\Phi = 2 \cdot 10^{14}$ n_{eq}/cm^2. Istraživanje prestavljeno u članku [36] slaže se s ovim rezultatom te tvrdi da CCE značajnije počinje opadati tek nakon apsorbirane doze više od $7 \cdot 10^{14}$ n_{eq}/cm^2. Maksimalna doza korištena u ovom radu manja je od navedene vrijednosti (186.75 kGy jednako je $5.60 \cdot 10^{14}$ n_{eq}/cm^2), pa ne iznenađuje da se posljedice zračenja još ne uočavaju TCT analizom uzoraka. Ponašanje detektora p-tipa također je u skladu s prijašnjim rezultatima [21], koji navode da CCE pada ispod 80 % tek nakon doze zračenja deset puta veće od maksimalne korištene u ovom radu.

Gama ozračivanje Czochralskog silicija uvodi pozitivni prostorni naboj u volumen detektora. To rezultira povećanjem efektivne gustoće prostornog naboja N_{eff} u detektorima n-tipa, odnosno njeno smanjenje u detektorima p-tipa. Prema jednadžbi (8.6), u potpuno osiromašenom detektoru V_{fd} proporcionalan je N_{eff}. To znači da će s povećanjem gama doze detektorima n-tipa napon potpunog osiromašenja rasti, a detektorima p-tipa opadati. Članak [9] opisuje kako se mijenja efektivno dopiranje N_{eff} u ovisnosti o apsorbiranoj dozi gama zračenja. Uz aproksimaciju maksimalne doze na 200 kGy, rezultate prikazane na slici 8.10 možemo iskoristiti za procjenu promjene vrijednosti V_{fd}:

$$\frac{V_{fd}(200kGy)}{V_{fd}(0kGy)} = \frac{N_{eff}(200kGy)}{N_{eff}(0kGy)} = \frac{3.5 \cdot 10^{12}}{3.4 \cdot 10^{12}} \approx 1.03. \tag{8.8}$$

Rezultati su prikazani u tablici 8.4. Očekivana promjena manja je od standardne pogreške TCT mjerenja, što znači da se evolucija vrijednosti napona potpunog osiromašenja ne može opaziti ovom metodom na korištenim dozama gama zračenja.

Jedina opažena posljedica zračenja bila je porast struje kroz detektor u reverznoj

	n-tip uzorak 4	p-tip uzorak 4
M1	225 V $\rightarrow$ 232 V	60 V $\rightarrow$ 58 V
M2	146 V $\leftarrow$ 150 V	77 V $\leftarrow$ 75 V
M3	121 V $\leftarrow$ 125 V	77 V $\leftarrow$ 75 V

Tablica 8.4: Evolucija vrijednosti V_{fd} kao posljedica ozračivanja detektora gama izvorom ^{60}Co. Gama zračenje uvodi pozitivni prostorni naboj u volumen detektora. Strelice pokazuju od izmjerenih prema predviđenim vrijednostima. S lijeve strane su vrijednosti V_{fd} u neozračenim detektorima, a s desne strane u ozračenim. Pretpostavljena je doza od 200 kGy.

polarizaciji. Potvrđena je poznata empirijska linearna ovisnost o apsorbiranoj dozi. Detektorima n-tipa ovo povećanje nije utjecalo na funkcionalnost, ali detektorima p-tipa onemogućilo je korištenje na sobnoj temperaturi. Ipak, od svih posljedica zračenja, povećanje struje najlakše je riješiti. Hlađenje uzoraka p-tipa omogućilo im je da dosegnu i do 200 V više napone, nego što je bilo moguće na sobnoj temperaturi. Uzorci p-tipa pokazali su se podložniji šumu.

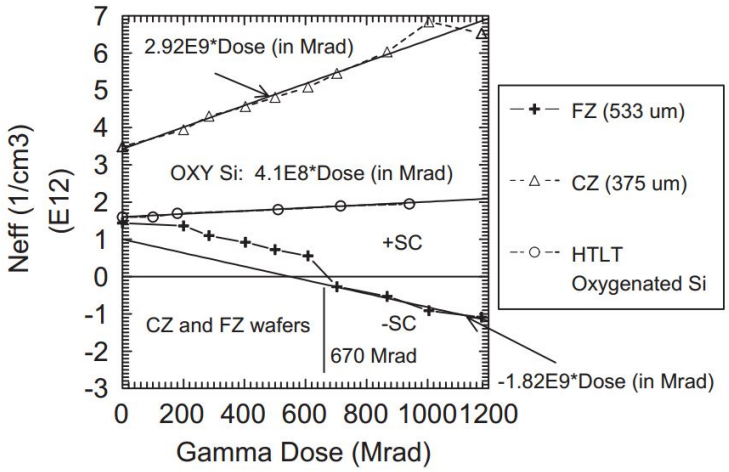

Slika 8.10: Efektivna gustoća prostornog naboja kao funkcija apsorbirane gama doze za silicijske detektore. Gama doze korištene u ovom radu padaju na sam početak X-osi (1 Mrad = 10 kGy).

Zaključno, uzorci n- i p-tipa demonstrirali su izdržljivost na doze gama zračenja do gotovo 200 kGy. Signali dobiveni TCT analizom crvenim laserom nisu ukazivali na degradaciju efikasnosti prikupljanja naboja. Promjene napona potpunog osiromašenja zbog uvođenja električki aktivnih defekata u volumen detektora bile su premale da bi se opazile TCT-om. Što se tiče porasta struje kroz detektore, uzorci n-tipa pokazali su se otpornijima od uzoraka p-tipa. I nakon najviše primijenjene doze ostali su pogodni za upotrebu na sobnoj temperaturi.

Bibliography

[1] Leo, W. R. Techniques for Nuclear and Particle Physics Experiments : A How-to Approach. 2nd revised ed. Berlin : Springer, 1994.

[2] Knoll, G. F. Radiation Detection and Measurement. 4th ed. USA : Wiley, 2010.

[3] Peltola, T. Design and construction of a transient current technique set-up and characterization of irradiated silicon detectors. Master's thesis. Espoo : Helsinki Institute of Physics, 2011.

[4] Moll, M. Development of radiation hard sensors for very high luminosity colliders — CERN-RD50 project. // Nuclear Instruments and Methods in Physics Research A. Vol. 511, 97-105 (2003).

[5] Tuovinen, E. Processing of radiation hard particle detectors on Czochralski silicon. PhD dissertation. Espoo : Helsinki Institute of Physics, 2008.

[6] Solid State Detectors – VII. Radiation Effects, USPAS-MSU Course, (2012.), Helmuth Spieler, http://www-physics.lbl.gov/~spieler/USPAS-MSU_2012/pdf/VII_Radiation_Effects.pdf, 22.5.2018.

[7] The Straggling function. Energy Loss Distribution of charged particles in silicon layers, (25.4.2012.), Stefano Meroli, http://meroli.web.cern.ch/Lecture_StragglingFunction.html, 22.5.2018.

[8] Winkler, A. D. Novel Detector Technologies for Medical Applications at the Example of Tumor Detection in BNCT. PhD dissertation. Helsinki : University of Helsinki, 2017.

[9] Li, Z. et al. Radiation hardness of high resistivity CZ Si detectors after gamma, neutron and proton radiations. // RD50 Workshop on radiation hard semiconductor devices for very high luminosity colliders 2003 / IEEE Nuclear Science Symposium Conference Record. Vol. 2, 1021-1027 (2003).

[10] Fundamental physical constants (Universal constants), (12.12.2017.), The NIST reference on Constants, Units and Uncertainty, https://physics.nist.gov/cgi-bin/cuu/Category?view=html&Universal.x=95&Universal.y=15, 22.5.2018.

[11] XCOM: Photon Cross Sections Database, (17.9.2009.), NIST, https://www.nist.gov/pml/xcom-photon-cross-sections-database, 22.5.2018.

[12] Thomson, M. Modern Particle Physics. 1st ed. Cambridge : Cambridge University Press, 2013.

[13] Lindström, G. et al. Radiation hard silicon detectors – developments by the RD48 (ROSE) collaboration. // Nuclear Instruments and Methods in Physics Research A. Vol. 466, 308-326 (2001).

[14] Fundamentals of Semiconductor physics: Energy bands, (23.3.2012.), Optics 4 engineers - Online courses, http://optique-ingenieur.org/en/courses/OPI_ang_M05_C02/co/Contenu.html, 15.6.2018.

[15] Electronic band structure, (28.4.2018.), Wikipedia, https://en.wikipedia.org/wiki/Electronic_band_structure, 15.6.2018.

[16] Muons in silicon (Si), (12.4.2018.), Particle Data Group, http://pdg.lbl.gov/2018/AtomicNuclearProperties/MUE/muE_silicon_Si.pdf, 16.6.2018.

[17] Hartmann, F. Evolution of Silicon Sensor Technology in Particle Physics. 1st ed. Berlin : Springer, 2009.

[18] Härkönen, J. et al. Processing of microstrip detectors on Czochralski grown high resistivity silicon substrates. // Nuclear Instruments and Methods in Physics Research A. Vol. 514, 173–179 (2003).

[19] Härkönen, J. Development of Radiation Hard Particle Detectors Made of Czochralski Grown Silicon. // Acta Physica Polonica A. Vol. 124, 372-376 (2013).

[20] Wu, X. et al. Strip Detectors Processed on High-Resistivity 6-inch Diameter Magnetic Czochralski Silicon (MCz-Si) Substrates. // IEEE Transactions on Nuclear Science. Vol. 61, 611-618 (2014).

[21] Casse, G. et al. Performances of miniature microstrip detectors made on oxygen enriched p-type substrates after very high proton irradiation. // Nuclear Instruments and Methods in Physics Research A. Vol. 535, 362-365 (2004).

[22] Lutz, G. Semiconductor Radiation Detectors: Device Physics. 2nd ed. Berlin : Springer, 2007.

[23] Härkönen, J. et al. Processing of $n^+/p^-/p^+$ strip detectors with atomic layer deposition (ALD) grown Al_2O_3 field insulator on magnetic Czochralski silicon (MCz-si) substrates. // Nuclear Instruments and Methods in Physics Research A. Vol. 828, 46-51 (2016).

[24] Härkönen, J. et al. Atomic Layer Deposition (ALD) grown thin films for ultra-fine pitch pixel detectors. // Nuclear Instruments and Methods in Physics Research A. Vol. 831, 2-6 (2016).

[25] Leskelä, M.; Ritala, M. Atomic layer deposition (ALD): from precursors to thin film structures. // Thin Solid Films. Vol. 409, 138-146 (2002).

[26] Suntola, T. Atomic Layer Epitaxy. // Materials Science Report. Vol. 4, 261-312 (1989).

[27] Sturm, J. M. et al. Imaging of oxide charges and contact potential difference fluctuations in atomic layer deposited Al_2O_3 on Si. // Journal of Applied Physics. Vol. 97, 063709 (2005).

[28] Härkönen, J. et al. The Cryogenic Transient Current Technique (C-TCT) measurement setup of CERN RD39 Collaboration. // Nuclear Instruments and Methods in Physics Research A. Vol. 581, 347-350 (2007).

[29] Fretwurst, E. et al. Investigation of damage-induced defects in silicon by TCT. // Nuclear Instruments and Methods in Physics Research A. Vol. 388, 356-360 (1997).

[30] Eremin, V. et al. Development of transient current and charge techniques for the measurement of effective net concentration of ionized charges (N_{eff}) in the space charge region of p-n junction detectors. // Nuclear Instruments and Methods in Physics Research A. Vol. 372, 388-398 (1996).

[31] Optical Absorption Coefficient Calculator, (N/A), BYU Cleanroom, `http://cleanroom.byu.edu/OpticalCalc`, 9.7.2018.

[32] Shockley, W. Currents to Conductors Induced by a Moving Point Charge. // Journal of Applied Physics. Vol. 9, 635-636 (1938).

[33] Ramo, S. Currents Induced by Electron Motion. // Proceedings of the IRE. Vol. 27, 584-585 (1939).

[34] He, Z. Review of the Shockley–Ramo theorem and its application in semiconductor gamma-ray detectors. // Nuclear Instruments and Methods in Physics Research A. Vol. 463, 250-267 (2001).

[35] Kramberger, G. et al. Determination of effective trapping times for electrons and holes in irradiated silicon. // Nuclear Instruments and Methods in Physics Research A. Vol. 476, 645-651 (2002).

[36] Härkönen, J. et al. Development of cryogenic tracking detectors for very high luminosity experiments. // Nuclear Instruments and Methods in Physics Research A. Vol. 607, 41-44 (2009).

[37] Particulars. Advanced measurement systems, (N/A), http://particulars.si/index.php, 22.6.2018.

[38] Cobalt-60, (13.5.2018.), Wikipedia, https://en.wikipedia.org/wiki/Cobalt-60, 20.5.2018.

[39] Photodisintegration, (9.1.2018.), Wikipedia, https://en.wikipedia.org/wiki/Photodisintegration, 20.5.2018.

[40] Rad (unit), (9.4.2018.), Wikipedia, https://en.wikipedia.org/wiki/Rad_%28unit%29#cite_note-remeffects-3, 20.5.2018.

[41] Tomić, P. Mjerenja perifernih doza za različite kolimatore gama noža. Diplomski rad. Zagreb : Prirodoslovno-matematički fakultet, 2016.

[42] Jackson, J. D. Classical electrodynamics. 3rd ed. USA : Wiley, 1998.